Science of the Total Environment 731 (2020) 139093

Contents lists available at ScienceDirect

Science of the Total Environment

journal homepage: www.elsevier.com/locate/scitotenv

Basin-wide responses of the South China Sea environment to Super Typhoon Mangkhut (2018)

Shuhong Liu [a,b], Jiagen Li [c], Liang Sun [c,**], Guihua Wang [d], Danling Tang [b], Ping Huang [f], Hong Yan [e], Si Gao [g], Chao Liu [a], Zhiqiu Gao [a], Yubin Li [a], Yuanjian Yang [a,b,e,*]

[a] School of Atmospheric Physics, Nanjing University of Information Science and Technology, Nanjing, China
[b] Guangdong Key Laboratory of Ocean Remote Sensing, South China Sea Institute of Oceanology, Chinese Academy of Sciences, Guangzhou, China
[c] School of Earth and Space Sciences, University of Science and Technology of China, Hefei, China
[d] Department of Atmospheric and Oceanic Sciences, Fudan University, Shanghai, China
[e] State Key Laboratory of Loess and Quaternary Geology, Institute of Earth Environment, Chinese Academy of Sciences, Xi'an, China
[f] Center for Monsoon System Research, Institute of Atmospheric Physics, Chinese Academy of Sciences, Beijing, China
[g] School of Atmospheric Sciences, Sun Yat-sen University, and Southern Marine Science and Engineering Guangdong Laboratory (Zhuhai), Zhuhai, China

HIGHLIGHTS

- Three significant-response regions were identified by multi-satellite observations.
- The daily growth rate of chl-a sped up considerably in non-shore areas.
- Sea surface salinity near the shore was dominated by asymmetric typhoon rainfall.
- Mangkhut-induced horizontal advection altered the environment of Beibu Gulf.
- Offshore upwelling in the southwest SCS was affected by the peripheral of Mangkhut.

GRAPHICAL ABSTRACT

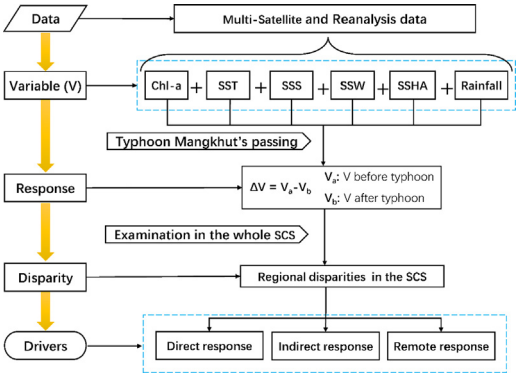

ARTICLE INFO

Article history:
Received 10 March 2020
Received in revised form 27 April 2020
Accepted 27 April 2020
Available online 04 May 2020

Editor: Fernando A.L. Pacheco

Keywords:
Chlorophyll-a bloom
Sea surface cooling
Multi-satellite remote sensing
Super typhoon Mangkhut

ABSTRACT

Relative to the open Northwest Pacific, the basin-scale South China Sea (SCS) is smaller and semi-enclosed, and the impacts of frequent super typhoons on the entire SCS basin have yet to be fully understood. Using multi-satellite observations and reanalysis data, this study explored biophysical responses of the upper ocean of the SCS induced by a typical super typhoon, Mangkhut (2018), and their regional differences with potential mechanisms. There were three different significant-response regions in the whole SCS, as follows: (1) In the ocean area around the typhoon path, strong vertical mixing, upwelling and cooling were induced, resulting in the surface chlorophyll-a (chl-a) concentration enhancing markedly (three-fold). Particularly, asymmetric distribution of typhoon rainfall induced asymmetric sea surface salinity change over along the path the nearshore. Diurnal peak of chl-a concentration increased obviously, and the daily growth rate of chl-a sped up considerably in non-shore areas after Mangkhut's passage. (2) In the Beibu Gulf (BBG), the peripheral winds of Mangkhut caused a change in direction of the sea surface flow field, transporting the high-temperature and high-salinity surface seawater from the southeastern area to the BBG. This induced dramatic increases in sea surface temperature, salinity

* Correspondence to: Y. Yang, School of Atmospheric Physics, Nanjing University of Information Science and Technology, Nanjing, China.
** Correspondence to: L. Sun, School of Earth and Space Sciences, University of Science and Technology of China, Hefei, China.
E-mail addresses: sunl@ustc.edu.cn (L. Sun), yyj1985@nuist.edu.cn (Y. Yang).

https://doi.org/10.1016/j.scitotenv.2020.139093

South China Sea

and height, and a decrease in chl-a, in most areas of BBG. (3) In the southwest SCS, the southwest monsoon–induced eastward offshore upwelling jet was weakened by the opposite large-scale peripheral wind vector of Mangkhut and gradually disappeared, resulting in accumulation and enhancement of chl-a in the nearshore. In addition, Mangkhut peripheral winds also intensified (weakened), shifting the cold (warm) eddy to the north (south) and blocking the horizontal eastward transport belt of the high-concentration chl-a. In general, our present work sheds light on the new evidence that a supper typhoon can cause basin-wide anomalies in the SCS, which has broad implications for marine biophysical environment.

1. Introduction

When a typhoon passes over the ocean, on the one hand it can bring severe weather such as strong winds, heavy rain, huge waves, storm surges and thunderstorms (Doong et al., 2011; Han et al., 2012, 2017), causing severe losses to coastal areas and maritime shipping (Cheng et al., 2012; Lagmay et al., 2015). Whilst on the other hand typhoon can cause intense air–sea heat and energy exchange (Lin et al., 2005; Price et al., 1994; Zhao et al., 2018) and a marked dynamical response of the upper ocean (Mei et al., 2015b; Price, 1981), which can help to maintain the global heat balance (Liu et al., 2008; Tu et al., 2011), further regulating regional and global climates (Guan et al., 2019; Liu et al., 2009; Wang et al., 2007), and even have important effects on marine ecological processes (Lin et al., 2003; Shang et al., 2008; Siswanto et al., 2008; Subrahmanyam et al., 2002). For instance, typhoon–ocean interaction can promote the proliferation of marine phytoplankton (Chiang et al., 2011; Huang and Oey, 2015; Shi and Wang, 2007, 2011), even causing the eruption of blooms (Shibano et al., 2011; Zhao et al., 2009; Zheng and Tang, 2007; Zheng et al., 2010), thereby increasing the oceanic primary productivity (Foltz et al., 2015; Huang and Oey, 2015; Liu et al., 2019); plus, it can also modulate the interannual variations in surface chlorophyll-a (chl-a) and oceanic primary productivity (Lin, 2012; Sun et al., 2010). Therefore, it is particularly important to monitor the abnormal changes in the upper environmental elements of the ocean [such as sea surface temperature (SST), the sea surface height anomaly (SSHA), sea surface wind (SSW), sea surface salinity (SSS), and chl-a] during typhoons.

Traditional marine in-situ observations and cruise surveys are often discontinued or absent during severe typhoon weather conditions, meaning an inevitable interruption to oceanic observations. However, with advancements in ocean satellite observation technology, satellite remote sensing has been widely used to observe the changes in the coastal ecological environment (Cham et al., 2020; Gholami and Baharlouii, 2019), and the biophysical responses of upper ocean to typhoons (Chacko, 2018; Liu et al., 2019; Solanki et al., 2008; Yue et al., 2018). For example, microwave remote sensing can penetrate the typhoon cloud layer to obtain real-time sea temperature changes, enabling us to gain a clearer understanding of the continuous changes in the ocean temperature field caused by a typhoon (Subrahmanyam, 2015; Wada et al., 2019; Wentz et al., 2000). With the help of advanced multi-source remote sensing methods, in the past 20 years, the impact of typhoons on the upper-ocean environment in the South China Sea (SCS), as the world's largest semi-enclosed marginal ocean, have also become much better understood. The SCS is located in the monsoon-affected area between the Pacific and Indian oceans. Due to its special geographical location and surrounding complex terrain, studies have shown that typhoons, as an important external factor in marine dynamic processes, can affect the stratospheric circulation in the SCS at multiple scales (Wang et al., 2009; Wang et al., 2019; Yu et al., 2019). Statistically, an average of about 10.3 typhoons hit the SCS each year, including typhoons moving westwards from an origin in the northwest Pacific (NWP) and those generated locally in the SCS (Fumin et al., 2002; Wang et al., 2007). Such a frequency of typhoons in the SCS is an important factor in the regulation of its ecological and physical environment (Chu et al., 2000; Lin, 2012; Mei et al., 2015a; Tang et al., 2014; Xu and Wang, 2017).

Previous studies have clarified that typhoons can cause local vertical mixing or entrainment and upwelling in the SCS, a lower SSHA, and transport cooler and higher-salinity seawater to the surface, resulting in deeper mixed layers and right-bias sea surface cooling (Sun et al., 2012, 2014; Yang et al., 2010; Zhang et al., 2014). Meanwhile, the intense mixing, upwelling and sub-mesoscale processes caused by the typhoon can bring deeper, nutrient-rich water from the subsurface to the surface light-transmitting layer, thereby promoting an increase in the chl-a concentration and oceanic phytoplankton/primary productivity, especially for pre-existing mesoscale cold oceanic eddy areas, where more substantial biophysical responses to typhoons are exhibited (Chen and Tang, 2011; Shang et al., 2015; Yang et al., 2012a; Zhao et al., 2009). In general, there are several main factors that influence the intensity of the upper-ocean response to a typhoon in the SCS, as follows: the typhoon's intensity, forcing time (translation speed and size in vortex diameter), pre-typhoon oceanic circulation, and mixed-layer depth (Lin et al., 2008; Mei and Pasquero, 2013; Sun et al., 2010; Zhao et al., 2008). For example, although Typhoon Hagbis (2007) in the SCS presented a very weak intensity, due to its looping path and slow translation speed, inducing a long forcing time for the local upper ocean, it caused local anomalous changes in the chl-a concentration at a climatic scale (Sun et al., 2010; Yang et al., 2012a). Relative to the tropical NWP, there was a shallower mixed layer (nutricline) and stronger subsurface thermal stratification (vertical nutrient gradient), resulting in much stronger SST cooling and surface chl-a bloom in the SCS basin when a typhoon passed (Mei et al., 2015a). However, previous studies on the oceanic impacts of typhoons in the SCS have been limited to certain areas under the influence of typhoons, especially those under or near the typhoon path.

In addition, the contribution of short-period, high-frequency physical changes (e.g., diurnal variation and various synoptic-scale weather conditions) is very important to ecological activities in the process of coupling physics and biogeochemistry (McCreary Jr et al., 2001; Picado et al., 2016; Ramos et al., 2013). Therefore, it is of great significance for marine ecological dynamics to explore the influence of typhoons on the diurnal variation in local chl-a concentrations in the SCS. Fortunately, the diurnal changes of phytoplankton can be perceived from the high-frequency sampling of geostationary ocean color satellites, which can make up for the lack of polar-orbit optical satellite remote sensing samples caused by the influence of clouds (Liu and Wang, 2016; Murakami, 2016; Wang et al., 2013, 2014). For example, the Himawari-8 geostationary satellite can provide hourly chl-a concentration products that can be used for short-term and long-term regional marine environmental monitoring (Murakami, 2016).

Therefore, there are two issues on the environmental responses to typhoons in the SCS, which has yet to be well understood, as followings: 1) relative to the open NWP, the SCS at the basin scale is smaller and the impact ranges of super typhoons are large. Therefore, it is unknown whether there are regional differences and different degrees of impact for identical super typhoons in the entire SCS basin. 2) Most previous studies have focused on changes in typhoons affecting the chlorophyll concentration of the oceans in the SCS within several days (e.g., Liu et al., 2019; Shang et al., 2015; Ye et al., 2013), leaving us a gap in

terms of the effects of typhoons on the diurnal variation of chl-a concentrations.

To address the two issues, in the present work, we mainly employed multi-source satellite remote sensing data and ocean reanalysis data to systematically analyze the anomalous impacts of super typhoons, as typified by super typhoon Mangkhut (No. 1822), on the entire SCS and their regional differences and potential causes. Typhoon Mangkhut, the strongest typhoon that landed in China in 2018, was characterized by a strong intensity, long duration of strong winds, wide range of wind and rain, and heavy impact, and thus it was a typical super typhoon passing over the SCS that can serve as a good case to study.

The rest of this paper proceeds as follows. In section 2, the various satellite data and methods used in our study are introduced. Section 3 examines the responses of the upper-ocean elements in different regions in the entire SCS basin to super typhoon Mangkhut and the potential mechanisms. Concluding remarks and discussion are given in Section 4.

2. Data and methods

2.1. Super Typhoon Mangkhut and study area

Super Typhoon Mangkhut was the twenty-second tropical storm and fourth super typhoon of the 2018 Pacific typhoon season. On September 5, 2018 (UTC), Typhoon Mangkhut generated over the NWP. The best-path data every six hours provided by the Joint Typhoon Warning Center are shown in Fig. 1. The data show that Mangkhut moved gradually westwards and achieved typhoon strength on September 9 with a central minimum pressure of 989 hPa and sustained winds of 65 kt (33.5 m/s). Thereafter, it continuously intensified. On September 11, Mangkhut reached super typhoon status, with a central minimum pressure of 919 hPa and sustained winds of 140 kt (72.2 m/s). The typhoon made landfall in Baggao, Cagayan, Philippines, at 1800 UTC on September 14. On September 15, it weakened into a typhoon and continued to move to the northwest. After passing over the northern SCS, the typhoon subsequently made landfall again at Jiangmen, Guangdong, China, on September 16. Following landfall, Mangkhut quickly weakened whilst moving westwards. Late on September 17, Mangkhut dissipated over Guangxi, China.

2.2. Satellite and reanalysis data

2.2.1. Chlorophyll-a

The Himawari-8 geostationary meteorological satellite was launched by the Japan Meteorological Agency in October 2014, and has been in operation since July 2015. It has a high spatiotemporal resolution and can return to the ground at a maximum spatial resolution of 2 km × 2 km every 10 min. The Advanced Himawari Imager is a multispectral imager with 16 channels, including three visible channels, three near-infrared channels and ten infrared channels, which can obtain visible and infrared images in the Asia-Pacific region. Because visible light limited by sunlight and cannot penetrate clouds, chl-a will have missing detections at night and under cloud-precipitation conditions. The chl-a concentration data used in this study were from the level-3 chl-a

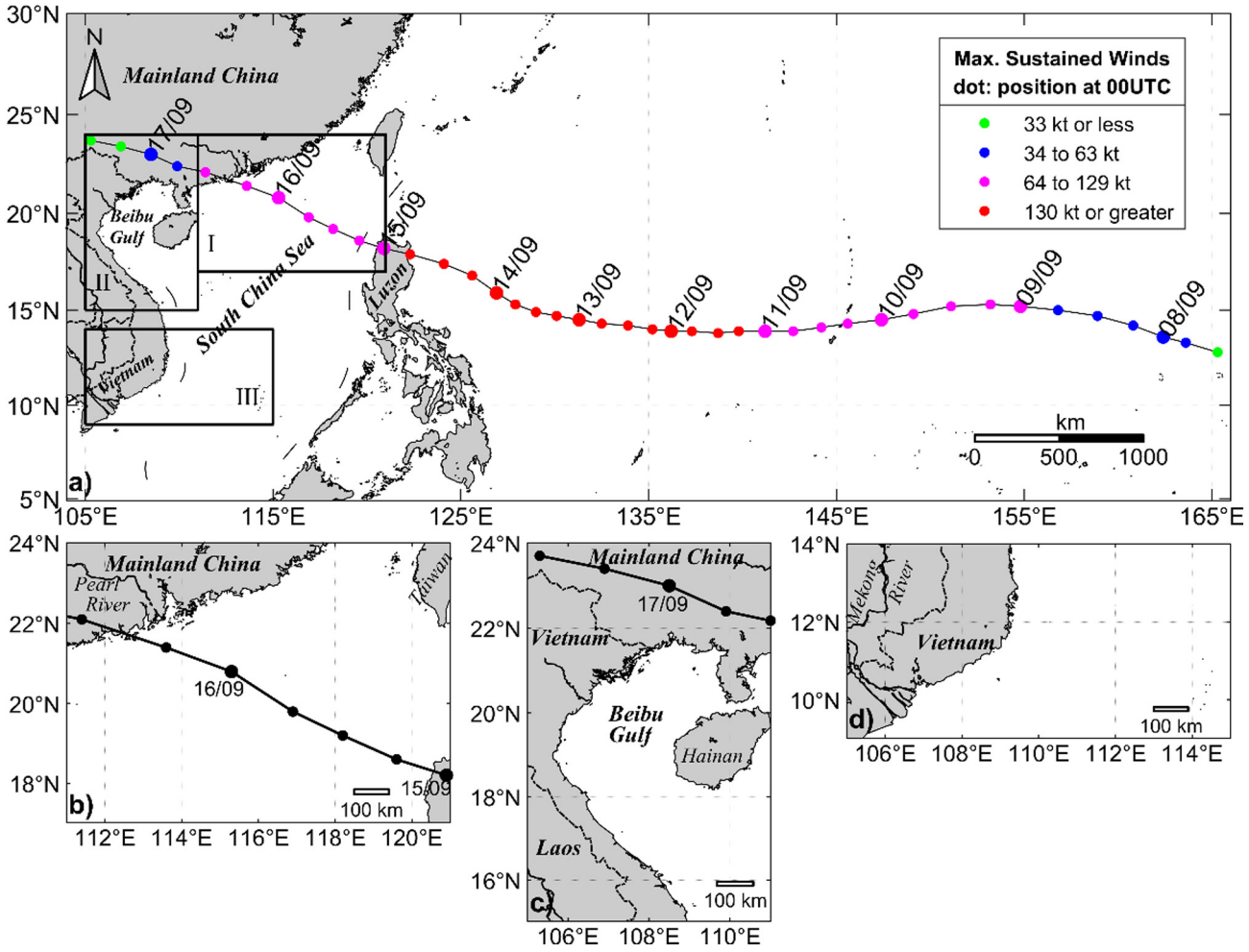

Fig. 1. Best track of super typhoon Mangkhut (2018) from the Joint Typhoon Warning Center. The track color indicates the maximum sustained wind of the typhoon. Also shown is the study area and the three different regions in the SCS affected by Mangkhut (black frames). (b-d) is the region I/II/III in (a).

concentration product obtained from the visible band of Himawari-8 (https://www.eorc.jaxa.jp/ptree/index.html), with a temporal resolution of 1 h and spatial resolution of 0.02° × 0.02° (Murakami, 2016).

2.2.2. Precipitation

The active weather radar is an important way for the detection of precipitation at large scale (Abdulrazzaq et al., 2019; Kuriqi, 2016; Yang et al., 2019). The Global Precipitation Measurement (GPM) mission is an international network of satellites based on the Tropical Rainfall Measuring Mission (TRMM), the TRMM data proved to be an effective tool to map the three-dimension distribution of precipitation (Abdulrazzaq et al., 2019; Yang et al., 2019). GPM carries the first satellite-borne Ku/Ka-band Dual-frequency Precipitation Radar and a multi-channel GPM Microwave Imager to improve the ability to measure light rain and provide global observations of rain and snow. This study used the final product from the Integrated Multi-satellite Retrievals for GPM, which combines data from all passive-microwave instruments in the GPM constellation and provides full coverage for the latitudes of 60°S–60°N. National Aeronautics and Space Administration's Precipitation Processing System publicly provided this product in March 2014 (https://pmm.nasa.gov/data-access/downloads/gpm). The precipitation data used were daily data with a spatial resolution of 0.1° × 0.1°.

2.2.3. Sea surface temperature

We used SST products that were integrated with microwave and infrared optimally-interpolated (MW_IR_OI) data. These can be obtained from Remote Sensing Systems (RSS) (www.remss.com). The MW_IR_OI data products used included the TRMM Microwave Imager, Advanced Microwave Scanning Radiomete, WindSat Polarimetric Radiometer and GPM microwave imager measured SST data. Also included were the SST data detected in the infrared band by the Moderate-resolution Imaging Spectroradiometer onboard the Terra and Aqua satellites of the Earth Observation Satellite series and the Visible/Infrared Imaging Radiometer Suite onboard the Suomi National Polar-orbiting Partnership.

Because sensors such as microwave imagers and microwave radiometers have the ability to penetrate clouds, and the infrared channel of polar-orbiting satellite radiometers has the characteristics of high spatial resolution, combining the two sets of data through optimal interpolation (i.e., MW_IR_OI) can overcome the impact of severe weather, such as excessive cloud cover, and perform all-weather observations to obtain high spatial resolution SST data, which is especially suitable when a typhoon is accompanied by a large number of clouds (Wentz et al., 2000). In this study, we used daily data with a spatial resolution of 9 km × 9 km.

2.2.4. Sea surface salinity

The SSS data were from the three-dimensional global ocean forecast product produced by the Copernicus Marine and Environmental Monitoring Service (CMEMS) Center's weakly coupled ocean–atmosphere data assimilation and forecast system (http://marine.copernicus.eu/services-portfolio/access-to-products/). The system uses a atmosphere configuration coupled with the ocean configuration and multi-thickness-category sea ice mode. This product includes daily mean files of temperature, salinity, currents, sea level, mixed-layer depth and sea-ice parameters (as well as hourly instantaneous SST, sea surface height and surface currents). The ocean observations of salinity assimilated include Argo, moored buoys and gliders. The SSS data used in this study were the daily data with a spatial resolution of 0.25° × 0.25°.

2.2.5. Sea surface height anomalies and surface geostrophic velocity

The SSHA and sea surface geostrophic velocity data, calculated based on geostrophic relationships, were satellite altimeter data from the Ssalto/Duacs multi-sensor gridded delay-time altimetry product provided by AVISO (Archiving, Validation and Interpretation of Satellite Oceanographic Data) (https://www.aviso.altimetry.fr/en/data/products/) and distributed by CMEMS. This product is processed from all satellite altimeter missions [Jason-3, Sentinel-3A, HY-2A, Saral/AltiKa, Cryosat-2, Jason-2, Jason-1, Topex/Poseidon, Environmental Satellite, Geosat Follow-On, European Remote Sensing satellites]. The spatial resolution of the SSHA and geostrophic data is 0.25° × 0.25° and the temporal resolution is 1 day.

2.2.6. Wind vector

The wind vector datasets were the wind at 10 m above the sea surface from the Cross-Calibrated Multi-Platform gridded surface vector winds provided by RSS. Cross-Calibrated Multi-Platform combines Version-7 RSS radiometer wind speeds, QuikSCAT and ASCAT scatterometer wind vectors, moored buoy wind data, and ERA-Interim model wind fields, and uses a variational analysis method to combine satellite observations and in-situ wind measurements into gap-free wind fields, for producing four maps daily of 0.25° gridded vector winds. Therefore, the temporal resolution of the wind field data used is 6 h and the spatial resolution is 0.25° × 0.25°.

2.2.7. Ekman pumping

In this research, we needed to calculate the upwelling (upw) caused by Ekman pumping. Price (1981) proposed the Ekman pumping formula as Eq. (1):

$$\mathrm{upw} = \nabla \times (\tau/\rho f), \tag{1}$$

where f is the Coriolis parameter, $\rho = 1020\ \mathrm{kg\ m^{-3}}$ is the density of seawater, and τ is the wind stress vector, which can be calculated by Eqs. (2) and (3) as follows:

$$\tau = \rho_a C_D |\mathbf{U_{10}}| \mathbf{U_{10}}, \tag{2}$$

$$C_D = \begin{cases} (4-0.6|\mathbf{U_{10}}|) \times 10^{-3} \ for\ |\mathbf{U_{10}}|<5\ \mathrm{m/s}; (0.737 + 0.0525|\mathbf{U_{10}}|) \times 10^{-3} \ for\ 5m/ \end{cases} \tag{3}$$

where $\rho_a = 1.26\ \mathrm{kg\ m^{-3}}$ is the air density, C_D is the drag coefficient (Jaimes and Shay, 2015; Powell et al., 2003), $\mathbf{U_{10}}$ is the 10-m wind vector. Various equations for calculating C_D over ocean surface have been proposed (Black et al., 2007; Powell et al., 2003; Price, 1981; See Text S1 in supplementary materials (SM)). In this context, the expression used in this research to compute C_D was based on recent results from field experiments in hurricanes which observed a saturation of C_D at wind speeds between 25 and 35 m/s (Donelan et al., 2004; Sanford et al., 2007; Vickery et al., 2009).

2.2.8. Eddy detection

According to previous studies (Lin et al., 2005; Shang et al., 2015; Shay et al., 2000), the SSHA was used as the basis for the determination of mesoscale eddies (Li et al., 2014, 2016). If there was a series of closed contours in the SSHA field, when the value of the outermost closed contour was >6 cm, the region was defined as a warm eddy; and when the outermost closed contour was less than −6 cm, the region defined was a cold eddy (Liu et al., 2017; Sun et al., 2019).

2.3. A flowchart of methodology

Fig. 2 shows the method flow of analyzing the effect of super typhoon Mangkhut on the upper ocean of SCS based on multi-satellite observations and reanalysis data.

Firstly, excepting for direct-derived variables, we employed SSW data to calculate the wind stress with Eqs. (2) and (3), and the upw with Eq. (1). Meanwhile, eddies were detected by using SSHA data. Particularly, we showed the rainfall distribution of the whole SCS during typhoon Mangkhut, which was closely related to SSS change.

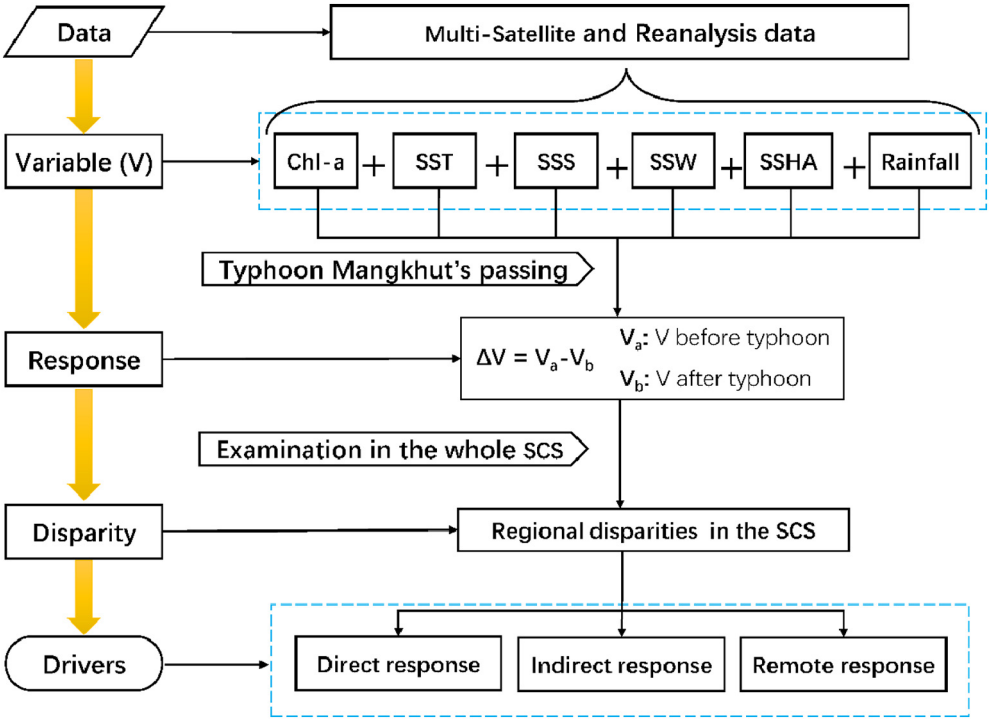

Fig. 2. Flowchart of analyzing the effect of super typhoon Mangkhut on the upper ocean of SCS.

Secondly, all of upw, SST, SSS and SSHA data were employed to calculate the difference before and after the typhoon Mangkhut, to obtain the physical response of the upper ocean. The difference in chl-a concentration before and after the passage of Mangkhut were used to analyze the biological response of the upper ocean.

Thirdly, we checked the changes of the biophysical environment in the whole SCS basin affected by Mangkhut's passage from 0000 UTC on September 15 to 1200 UTC on September 17. Three distinct biophysical response regions shown in Fig. 1 were found as follows: Region I: direct response region, i.e., along the track of Typhoon Mangkhut (17°-24°N, 111°-121°E); Region II: indirect response region, i.e., Beibu Gulf (BBG) (15°–24°N, 105°–111°E); Region III: remote response region, i.e., offshore of southern Vietnam in the southwest SCS (9°–14°N, 105°–115°E).

Finally, the potential drivers for the direct, indirect and remote responses to typhoon Mangkhut were comprehensively examined.

3. Results

3.1. Typhoon Mangkhut–induced strong wind, Ekman pumping and precipitation in the SCS

Super typhoon Mangkhut caused strong winds and severe rainfall over the SCS. The wind vector diagram shows that the wind in the northern part of the SCS was weak (<11 m/s) on 13 September 2018 before Mangkhut entered the SCS (Fig. 3a). During 14–17 September, affected by the typhoon (Figs. 3b–3i), strong winds prevailed in the northern part of the SCS, and the maximum wind speed exceeded 30 m/s (Fig. 3d). Fig. 3 also describes the local upwelling of the SCS within a few hundred kilometers caused by the typhoon calculated by the wind field according to Eqs. (1)–(3). The range of the upwelling speed was 0.2×10^{-4} to 8×10^{-4} m/s, and the maximum value of upwelling reached 8×10^{-4} m/s on September 15 (Fig. 3d). Note in particular that the intensity of the upwelling caused by the typhoon was greater on the right-hand side of the path than on the left-hand side, due to the asymmetric wind stress (Chang et al., 2008; Price, 1981; Yue et al., 2016).

The distributions of average daily rainfall in the SCS for the whole period of Mangkhut were shown in Figs. S1a-1f in SM and 4a-c. Before the passage of Mangkhut, the average daily rainfall in the northern part of the SCS was generally <20 mm/day [Fig. S1a]. During Mangkhut's period, however, a large amount of rainfall occurred near the typhoon path, and the heavy precipitation was mainly located in the internal spiral rain about 50 km from the typhoon center. The heavy rainfall (>120 mm/day) zone corresponded to the strong-wind zone (Fig. 3); in particular, the daily rainfall in the area near the left-hand side of the typhoon path increased by 10–15 times relative to that before Mangkhut (Fig. 4a), clearly showing the asymmetric rainfall distribution on September 16, 2018 (Fig. 4c). That is, the rainfall was stronger on the left-hand side of the path than on the right-hand side, which coincides with the findings of previous studies (Chan et al., 2019; Zhao et al., 2009; Zheng and Tang, 2007). Rainfall asymmetry is mainly related to various potential environmental factors, including tropical cyclone intensity and motion, vertical wind shear, terrain, SST, and precipitable water vapor (Chan et al., 2019; Corbosiero and Molinari, 2003; Gao et al., 2018). According to the rainfall distribution, it can be seen that the rainfall in the vicinity of the typhoon path mainly appeared during September14–16, 2018 (Fig. 4a–c), while the Beibu Gulf area was affected by the typhoon rainfall on September 17–18, 2018 (Fig. S1e-S1f).

3.2. Biophysical response of the upper ocean along the track of Typhoon Mangkhut

3.2.1. Physical response

Typhoon Mangkhut had a direct impact on the upper ocean along its track. Fig. 4d-f shows SST differences after and before the typhoon along the track of typhoon Mangkhut. Before typhoon Mangkhut, the northern SCS mainly had a warm ocean surface of 28 °C–30 °C (Fig. S2a-S2b in SM). On September 15, 2018, Mangkhut began to affect the northern part of the SCS, causing a cold wake via vertical mixing and Ekman pumping (Fig. 3; Price, 1981). During September 16–18, 2018, dramatical patches of large-scale sea surface cooling occurred (Fig. 4d–f), which is in line with the results previous studies (Chacko, 2017; Subrahmanyam, 2015; Yue et al., 2018). In detail, the lowest

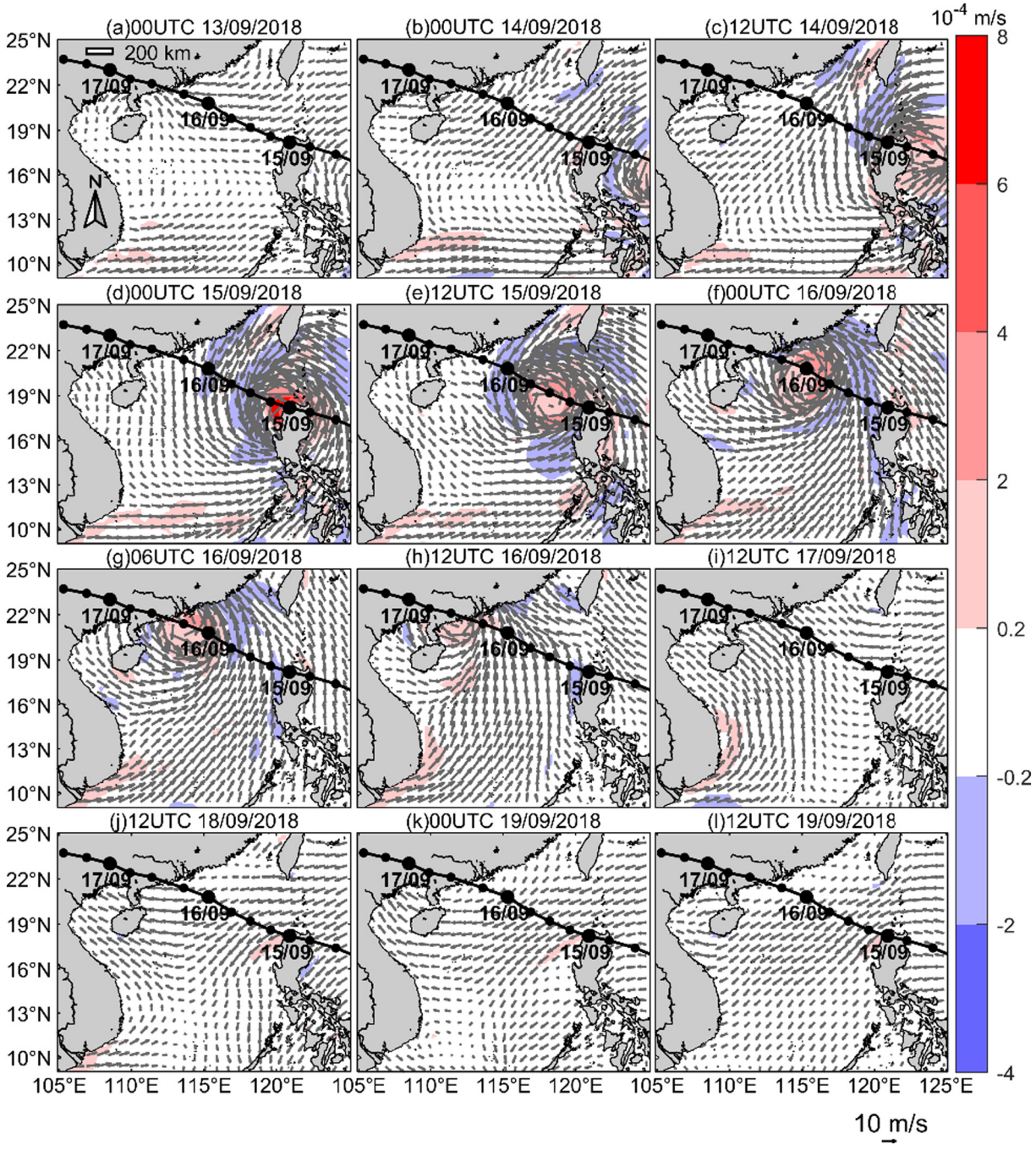

Fig. 3. The wind fields at 10 m (arrows) and the Ekman pumping velocity (shaded, positive value is upwelling) in the SCS during the passage of Typhoon Mangkhut.

SST of 25 °C appeared on the right-hand side of the typhoon path, with a maximum sea surface cooling of −2.8 °C (Fig. 4d). This right-hand side bias in SST cooling would have been mainly caused by asymmetric wind stress (Price, 1981; Shi and Wang, 2011), and partly by a greater surface latent heat flux owing to the greater wind speed on the right-hand side of the typhoon path (Gao and Chiu, 2010).

Fig. 4g-i shows obvious changes in SSS caused by typhoon Mangkhut. Specifically, the salinity mainly ranged from 32.5 to 33.5 psu before the passage of the typhoon (Fig. S3 in SM), and then an increase in SSS of 1 psu occurred on the right-hand side of the typhoon path in the offshore area after the passage of Mangkhut (Fig. 4h–i). In previous studies, sea surface salinity also increased after typhoon derived by Ship-measurement (Zheng and Tang, 2007). This is because the stronger upwelling would have brought more high-salinity water from the subsurface to the surface, caused by stronger wind stress, and there was less rainfall on the right-hand side of the path relative to the left-hand side (Figs. 3, 4a-c and g–i). In contrast, the stronger rainfall and weaker upwelling were unfavorable to an increase in SSS on the left-hand side of the path in the offshore area (Fig. 4g–i). Particularly, in the nearshore, the much stronger rainfall and runoff from the mainland to the coastal area on the left-hand side on September 16 would have been favorable for desalination of the sea surface water (Fig. 4c); and this, together with the relatively lower salinity of the entire layer of seawater, meant there were significant decreases in SSS of 1 psu after the typhoon (Fig. 4g–i). In summary, the change in SSS caused by the typhoon on both sides of its path was mainly determined by a mechanism of competition between the

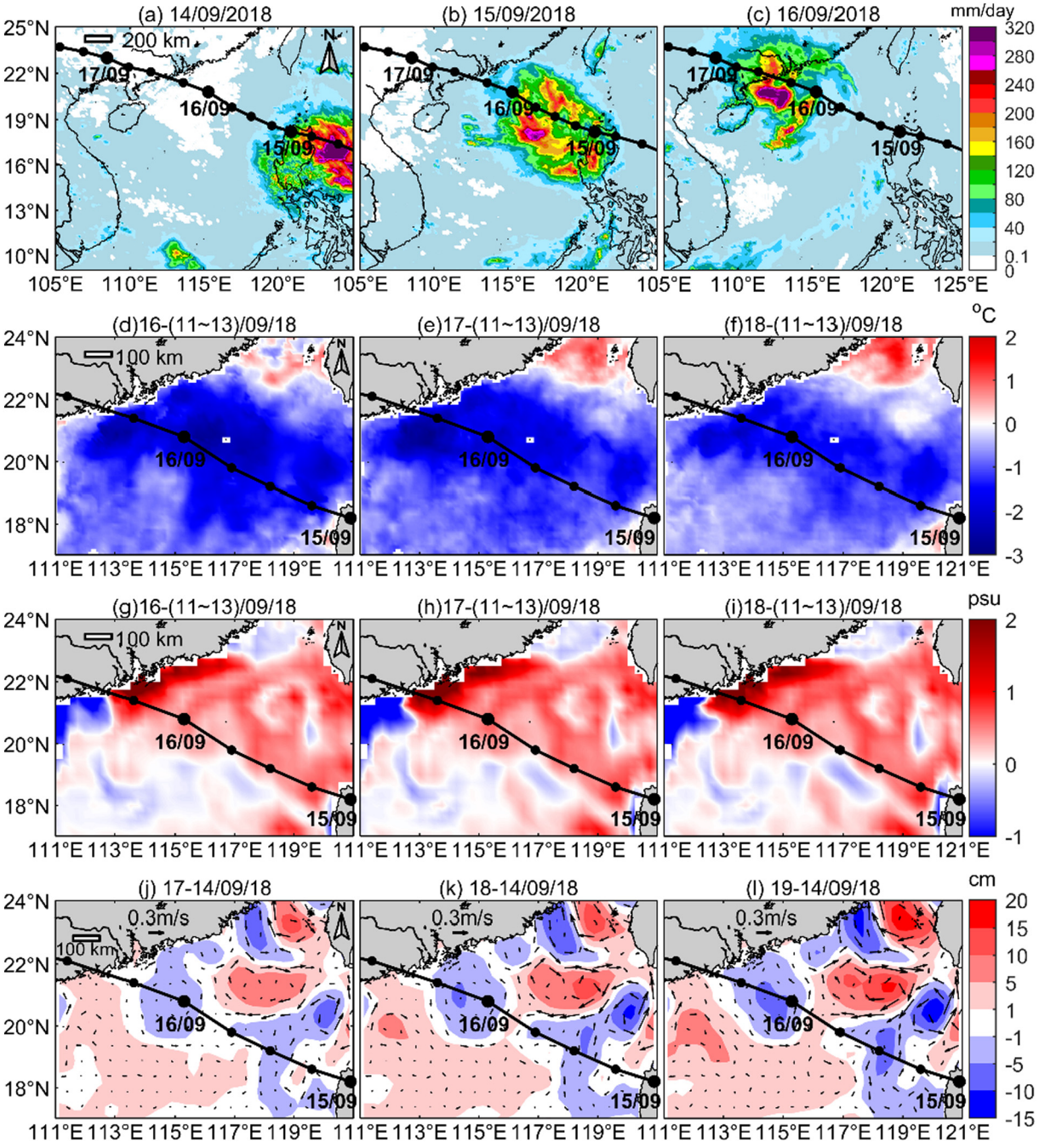

Fig. 4. Evolution of daily precipitation in the SCS, and physical response of the upper ocean in region I during the passage of typhoon Mangkhut: (a-c) daily precipitation on September 14–16, 2018; (d-f) the SST (shaded, °C) difference between September 16/17/18 and the average of September 11–13, 2018; (g-i) the SSS (shaded, psu) difference between September 16/17/18 and the average of September 11–13, 2018; (j-l) the altimeter-derived SSHA (shaded, cm) difference and surface geostrophic velocity (arrows) difference between September 17 and 14, 2018.

asymmetric typhoon precipitation and upturned high-salinity subsurface water caused by Ekman pumping.

Fig. 4j-l shows the evolution of the SSHA and sea surface flow fields before and after the passage of typhoon Mangkhut. A positive SSHA was the main pre-existing oceanic feature along the path. There was a warm eddy (22°N, 116°E) before the typhoon on the right-hand side of the typhoon path (Fig. S4a in SM). Then, after Mangkhut had passed, with the decrease in the SSHA, the warm eddy gradually weakened and disappeared on September 19 (Fig. S4b-S4f in SM). In addition, the position where the SSHA was reduced (21° N, 116° E) (Fig. 4j) corresponded to the position of maximum SST cooling (Fig. 4d), indicating that the largest decrease in SSHA can indicate the location where the maximum drop in SST occurred.

3.2.2. Biological response

In the tropical oceans, limited nutrient concentrations in the upper ocean are not conducive to enhancing primary productivity, which can be indicated by the variations in chl-a concentrations in phytoplankton (Bai et al., 2005; Lomas et al., 2012). Typhoon-induced upwelling and vertical mixing, which can be indicated by strong SST cooling, will bring relatively more phytoplankton and richer nutrients from the subsurface to the sea surface layer; and together with the usually sufficient sunshine and strong photosynthesis after the passing of a typhoon,

there can be a marked increase in the surface chl-a concentration (Chacko, 2017; Lin et al., 2003; Liu et al., 2019; Ye et al., 2013).

Figs. 5a and b show the changes in the concentration of chl-a before (September 6–13, 2018) and after the passage of Typhoon Mangkhut (September 18–19, 2018). The high concentration of chl-a of >0.3 $mg \cdot m^{-3}$ in the nearshore areas would have been mainly due to the influence of terrestrial material brought by land surface runoff and diluted water, resulting in second-class water bodies with severe eutrophication in the coastal areas of the mainland (Tang et al., 2003, 2004a, 2006; Zheng and Tang, 2007). In the nearshore, especially, the heavy precipitation induced by Mangkhut that appeared on the left-hand side of the path (Fig. 4c) would have increased the level of river-water dilution and coastal runoff, and large quantities of nutrients would have been transported into the coastal areas of the mainland, contributing to the increase in the chl-a concentration, which is consistent with the findings of a previous study (Zheng and Tang, 2007). In the offshore areas, the concentration of chl-a along the path ranged from 0.01 to 0.1 $mg \cdot m^{-3}$ (Fig. 5a) before Mangkhut's passage. After its passage, however, the concentration increased by 0.02–0.3 $mg \cdot m^{-3}$ (Fig. 5c), and the maximum concentration of chl-a on the right-hand side of the path exceeded 0.4 $mg \cdot m^{-3}$, with a three-fold maximum increase. Compared with Fig. 4d-f, area A (black frame in Fig. 5a), where the maximum chl-a concentration increased, coincided with the area where the maximum SST decreased with the "cold wake" (Fig. 4d) and the upwelling sea (Fig. 3e).

Fig. 5d shows the diurnal variations in the hourly chl-a concentration averaged within area A during 0900–1600 (local standard time, LST = UTC + 8) during September 6–23, 2018. As can be seen, there was a similar diurnal phase of the chl-a peak before and after the typhoon, whereas there were higher concentrations of chl-a with a higher peak of >0.25 $mg \cdot m^{-3}$ after the typhoon. Specifically, there was little obvious change from 0900 LST to 1400 LST, and then the sharp increase began after 1400 LST. This is because of the sufficient sunlight in the afternoon, whereby phytoplankton would have grown gradually during the daytime and accumulated chl-a through photosynthesis, leading to the subsequent enhancement in the chl-a concentration in the afternoon. To verify the growth rate of chl-a, Table 1 shows the rate of change in the chl-a concentration during 0900–1600 LST and 1200–1600 LST. It can be seen that the chl-a concentration changed to a high level in the afternoon both before and after the typhoon, when sunlight was abundant, and there was an increase in the chl-a concentration. This differs from the results of Wang et al. (2014) who found that the changes in the chl-a concentration in the East China Sea and the Bohai Sea during 0900–1600 LST first grew and then declined.

Table 1
Rate of change in chl-a concentration during 0900–1600 LST and 1200–1600 LST.

Date	During 0900–1600(LST) chl-a variation rate ($mg \cdot m^{-3} \cdot h^{-1}$)	During 1200–1600(LST) chl-a variation rate ($mg \cdot m^{-3} \cdot h^{-1}$)
6–13/09/2018	0.016	0.032
18/09/2018	0.023	0.040
19/09/2018	0.005	0.008
20/09/2018	0.015	0.030
21/09/2018	0.024	0.039
22/09/2018	0.015	0.025
23/09/2018	0.012	0.019

Particularly, in the offshore SCS after the typhoon (September 18–19), the concentration of chl-a was highest on September 18, which is consistent with previous findings that there were usually delays of a few days for the growth of chl-a to the maximum (Gierach and Subrahmanyam, 2008; Zheng et al., 2010). More evidently, the daily rate of change was higher, with 0.023 $mg \cdot m^{-3} \cdot h^{-1}$ during 0900–1600 LST, and the highest growth rate was 0.040 $mg \cdot m^{-3} \cdot h^{-1}$ during 1200–1600 LST. This would have been due to the typhoon-induced vertical mixing (or entrainment) bringing subsurface phytoplankton and rich nutrients to the surface layer, resulting in a chl-a bloom. After September 20, 2018, the elevated nutrients would have begun to be gradually used up, and about one week after the typhoon (September 23, 2018), the concentration of chl-a and its diurnal growth rate had decreased to the original level of chl-a.

3.3. Response of Beibu Gulf

Before the passage of Mangkhut, the SST of the BBG was around 29 °C, which was 1 °C lower than that to the southeast of the BBG (Fig. S5a in SM). When Mangkhut passed on September 17, 2018, it also affected the upper ocean of the BBG. The wind field at 10 m was affected by the typhoon on September 17 (Fig. 3i), and the wind direction turned northerly to southerly (Fig. 3h and i). The southerly wind may have been favorable for the high-SST water (16°N–18°N) to be gradually blown to the BBG during 17–19 September 2018, thereby increasing the SST by 1 °C in most areas of the BBG (Fig. 6a–b).

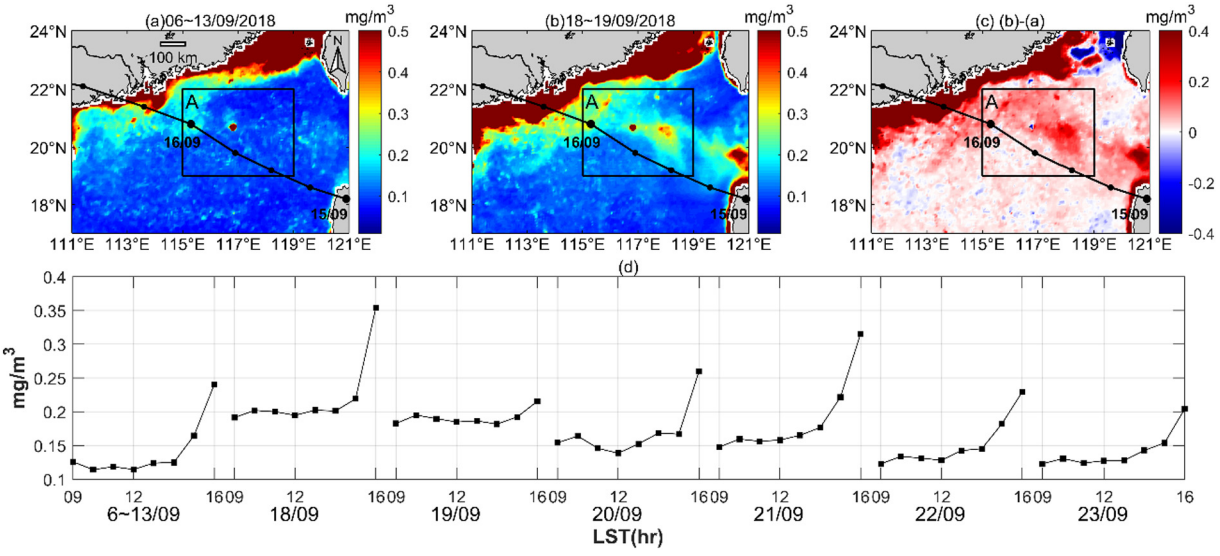

Fig. 5. Variation in the chl-a concentration in region I before and after typhoon Mangkhut: (a) the mean chl-a concentration during September 6–13, 2018; (b) the mean chl-a concentration on September 18 and 19, 2018; (c) the chl-a concentration difference between the mean value on September 18 and 19, 2018 and the mean value during September 6–13, 2018; (d) the hourly change during the daytime (per day from 0900 to 1600 LST, LST is UTC + 8) of the mean chl-a concentration in the black frame (region A) before and after the typhoon.

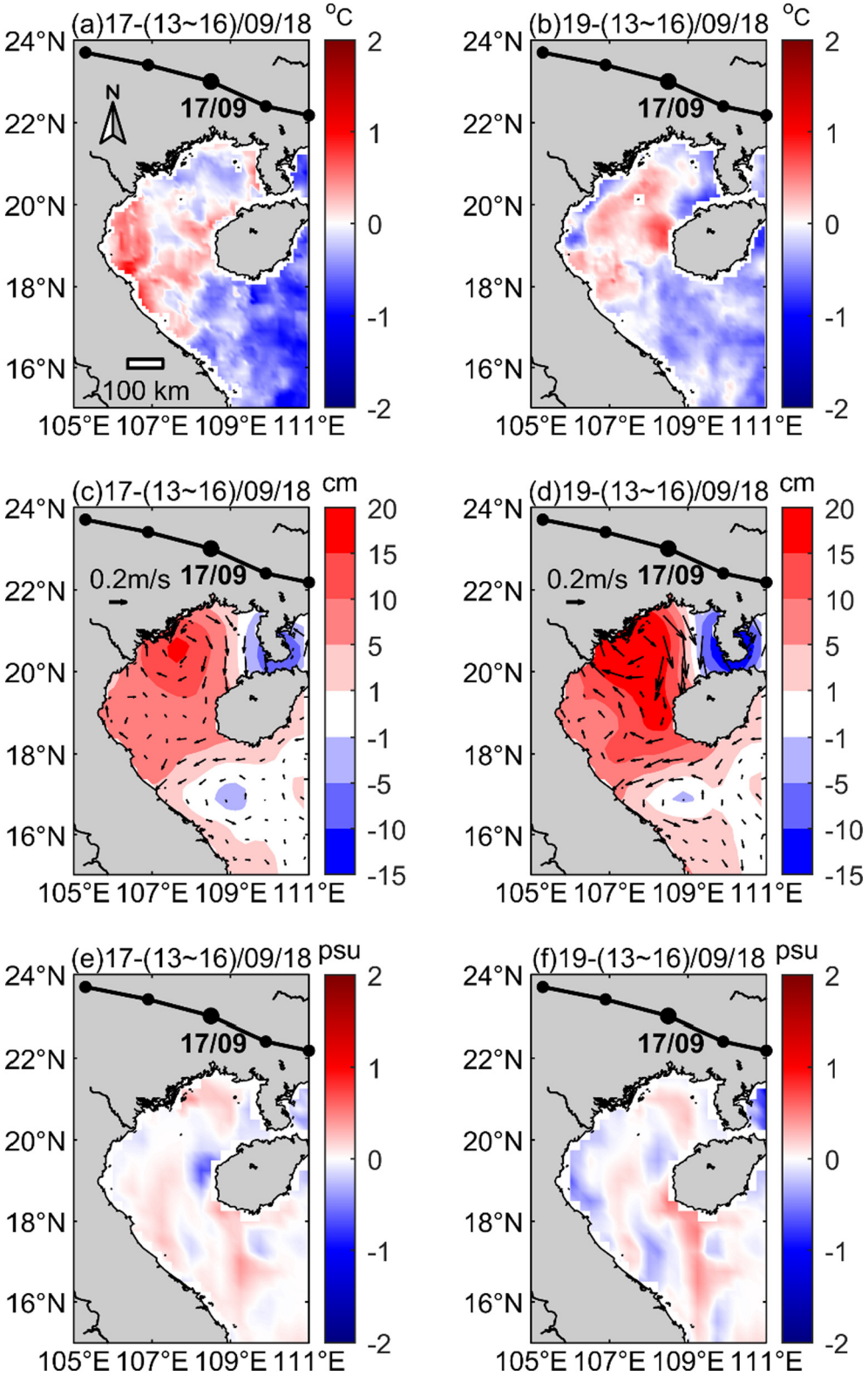

Fig. 6. Physical response of the upper ocean in region II during the passage of typhoon Mangkhut: (a-b) the SST difference between September 17/19 and the average of September 13–16, 2018; (c-d) the SSHA (shaded, cm) difference and surface geostrophic velocity (arrows) difference between September 17/19 and the average of September 13–16, 2018; (e-f) the SSS (shaded, psu) difference between September 17/19 and the average of September 13–16, 2018.

To address this transboundary high-SST phenomenon, Fig. 6c-d shows the difference of the SSHA and sea surface flow fields before and after Mangkhut. Before the passage of typhoon Mangkhut, there was a warm anticyclone eddy with an SSHA of ~20 cm (Fig. S6a in SM). During 17–19 September 2018, the southerly peripheral wind vectors of Mangkhut were favorable to drive the outside sea surface flow into the BBG, intensifying the pre-existing warm eddy and expanding it northwards (Fig. S6b-d in SM). The SSHA increased by 10–20 cm and the maximum SSHA increase exceeded 20 cm in the BBG (Fig. 6c–d). On September 13–16, 2018, the high-temperature

water near the area (17.5°N, 108.5°E) could have been brought into the BBG by the sea surface anticyclonic current (Fig. S5a in SM). Therefore, the increased SST firstly appeared in the nearshore of the southern BBG, and then expanded into most other areas of the Gulf (Fig. 6a and b).

The SSS also showed a similar response as the SST; the southeastern high-salinity water was transported along with the anticyclonic sea surface current into the BBG (Fig. 6e-f). This resulted in a slight increase in most areas of the BBG during 17–19 September 2018 (Fig. 6e and f). Meanwhile, the salinity decreased in certain parts of the BBG (Fig. 6f), probably caused by the typhoon precipitation (Fig. S1f in SM).

In terms of the biological response, there was also a clear response of the chl-a concentration in the BBG. Before the passage of Mangkhut, there were high chl-a concentrations of >0.3 $mg \cdot m^{-3}$ in most Gulf areas, especially for the coastal areas (>0.5 $mg \cdot m^{-3}$) (Fig. 7a), possibly because of the nutrients delivered by the runoff from coastal cities and some small rivers that discharge into the Gulf, or from regional upwelling and tidal mixing (Tang et al., 2003), and the presence of mangroves in the coastal zone also ensure the concentration of chl-a (Gholami and Baharlouii, 2019). After the passage of typhoon Mangkhut, there was a significant decrease in the chl-a concentration along the coast and western parts of the Gulf (Fig. 7b), by about 0.2–0.4 $mg \cdot m^{-3}$ (Fig. 7c). This can also be explained by the fact that the lower chl-a water would have been transported there along the anticyclonic current. In contrast, there was a significant increase in the chl-a concentration in the northeast part of the Gulf, which was probably caused by typhoon-induced regional upwelling and mixing as well as runoff from the mainland (Tang et al., 2003; Zheng and Tang, 2007).

3.4. Response of offshore upwelling in the southwest SCS

For the wind field and Ekman upwelling distribution (Fig. 3), it can be seen that South Vietnam offshore upwelling existed in the southwest SCS before the typhoon, which is consistent with the observed fact in September from previous studies (Tang et al., 2004b, 2006; Yang et al., 2012b). Generally, because the prevailing southwest winds in the SCS in summer were blocked by the north–south Annam Cordillera mountain range (Dippner et al., 2007; Wang et al., 2006; Xie et al., 2003, 2007), the offshore upwelling was formed in June, and its intensity reached its peak in July–September, before gradually disappearing in October (Da et al., 2019; Kuo et al., 2000; Tang et al., 2006; Yang et al., 2012b). At the same time, the western boundary currents were superimposed in the southwest SCS, making the offshore upwelling transport eastwards at about 11.5°N, resulting in an offshore chl-a bloom jet (Chen et al., 2012; Dippner et al., 2007; Wang et al., 2019). During the passage of Mangkhut, the offshore upwelling was affected by the combination of the peripheral wind vectors of Mangkhut and the southwest monsoon. During 13–14 September 2018, the offshore upwelling strengthened and transported eastwards. Then, from September 15, 2018, when the typhoon entered into the SCS, the offshore upwelling gradually weakened and finally transported northwards along the continental Vietnam shelf (Fig. 3e–i). After the typhoon had dissipated, the offshore upwelling gradually disappeared (Figs. 3j–l).

Correspondingly, Fig. 8 shows the daily changes of the SSHA and sea surface flow fields in the southwest SCS, indicating that there was a cold cyclonic eddy and a warm anticyclonic eddy. There was an offshore flow from west to east between the cold eddy and the warm eddy, which corresponded to the location of the offshore upwelling. Due to the peripheral wind vectors of Mangkhut being opposite to the monsoon vectors on 14, 15, and 19 September, the cold eddy strengthened and expanded southwards, while the warm eddy weakened and expanded southeastwards (Fig. 8h–k), which further blocked the eastward offshore upwelling.

Fig. 9 shows the distribution of chl-a concentration before and after the impact of Mangkhut in area III. It can be seen that the concentration of chl-a along the estuary of the Mekong River was significantly higher than that of the open sea. The concentration of chl-a near the estuary of the Mekong River was >1 $mg \cdot m^{-3}$, while the concentration in the offshore area was generally lower than about 0.5 $mg \cdot m^{-3}$. This spatial pattern of chl-a value was also validated by the multi-year satellite observations (Tang et al., 2004b, 2006; Yang et al., 2012b). Before typhoon Mangkhut (September 10–13, 2018), the average chl-a concentration distribution showed a high chl-a jet in area B; whereas after the typhoon (September 18–19, 2018), the chl-a jet disappeared, due to the disappearance of offshore upwelling as mentioned above. Meanwhile, the accumulation of high-value areas of chlorophyll near the shore was enlarged, due to the eastward transportation of chl-a blocked by the southward-shifted cold eddy. In general, typhoon Mangkhut had a strong intensity and a large area of impact in the SCS. It not only affected the ocean near the typhoon path, but also the marine environment in areas far from the typhoon path through the interaction with the monsoon.

4. Conclusions and discussions

4.1. Conclusions

Super typhoon Mangkhut generated in the NWP in September 2018. Based on multi-satellite remote sensing observation data combined with ocean reanalysis data, the present work systematically and comprehensively examined the response of the marine environment in the SCS to typhoon Mangkhut. Since the scale of the SCS is relatively

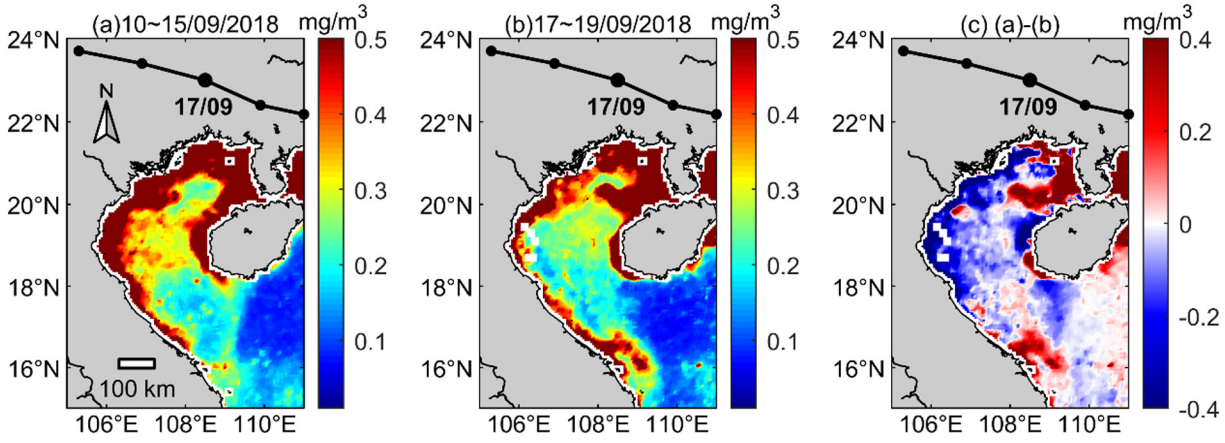

Fig. 7. Variation in the chl-a concentration in region II before and after typhoon Mangkhut: (a) the mean chl-a concentration during September 10–15, 2018; (b) the mean chl-a concentration during September 17–19, 2018; (c) the chl-a concentration difference between the mean value during September 17–19, 2018 and the mean value during September 10–15, 2018.

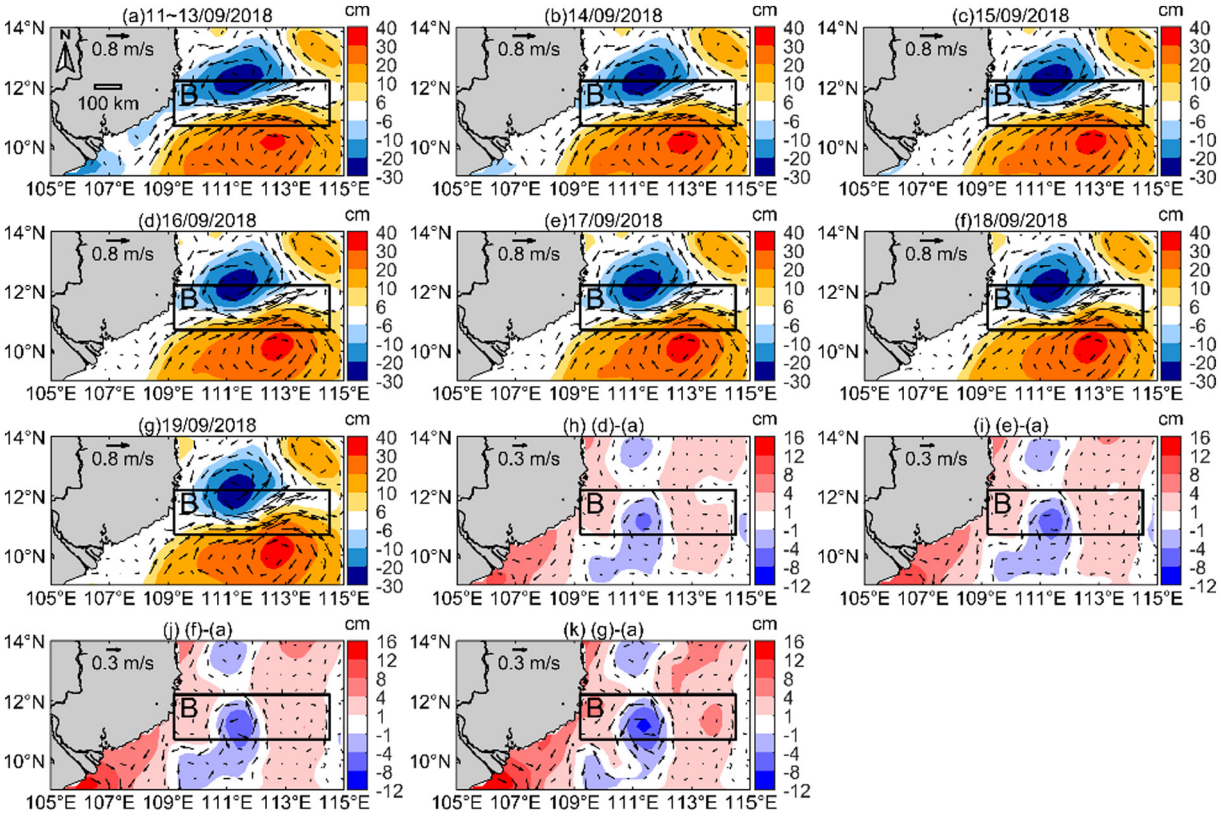

Fig. 8. Evolution of the SSHA (shaded, cm) and surface geostrophic velocity (arrows) in region III during the passage of typhoon Mangkhut: (a) the mean SSHA and geostrophic velocity during September 11–13, 2018; (b–g) the daily SSHA and geostrophic velocity during September 14–19, 2018; (h) the SSHA difference between September 16 and the mean value of geostrophic velocity during 11–13 September 2018; (i) the SSHA difference between September 17 and the mean value of geostrophic velocity during September 11–13, 2018; (j) the SSHA difference between September 18 and the mean value of geostrophic velocity during September 11–13, 2018; (k) the SSHA difference between September 19 and the mean value of geostrophic velocity during September 11–13, 2018.

small compared to the open ocean, super typhoons have different degrees of influence on the oceans in the SCS at different distances from the typhoon center. The different impacts of typhoon Mangkhut on the SCS basin can be summarized as three types (as shown in Fig. 10): direct impact (area I), indirect impact (area II), and remote impact (area III). The main conclusions can be summarized as follows:

In area I (along the typhoon track), the upper ocean in the northern part of the SCS near the typhoon track produced a complex response to the direct forcing of typhoon Mangkhut. Most of the phenomena are consistent with the open-ocean observations of previous studies. Due to the entrainment and upwelling of the typhoon during September 14–16, 2018, the subsurface cold and high-salinity seawater was brought to the surface, resulting in a decrease in SST (up to 2.8 °C) and increase in salinity (about 1 psu) in the nearshore after the typhoon. The SSS was mainly determined by the upturned high-salinity seawater (Fig. 10). In the nearshore, due to the asymmetry of precipitation (>240 mm/day on the right of the track and < 200 mm/day on the left of the track) and the relatively lower salinity of the entire layer of seawater, the SSS decreased markedly by 1 psu on the left-hand side of the typhoon path (Fig. 10). It can be seen from the above that the typhoon-induced SSS variation on both sides of the path was mainly determined by a mechanism of competition between the typhoon precipitation and enhanced salinity from subsurface water associated with upwelling and vertical mixing.

Meanwhile, using geostationary satellite data, we have discovered the diurnal variation process of chlorophyll growth under the influence of typhoons as follows. The vertical mixing brought by the typhoon brought phytoplankton and nutrients to the surface of the ocean, which enhanced the oceanic primary productivity. The maximum increase in chl-a concentration was roughly three-fold (Fig. 10). Note that on both the day before and after the typhoon, the accumulation of chl-a concentration reached its maximum at around 1600 LST, but the growth rate of the daily change in the concentration of chl-a after the typhoon was greater than that before. Therefore, although a typhoon will not change the diurnal trend of the chl-a concentration, it will bring more phytoplankton and nutrients into the upper ocean, together with more suitable phytoplankton photosynthesis, thus increasing the daily growth rate and peak value of chl-a.

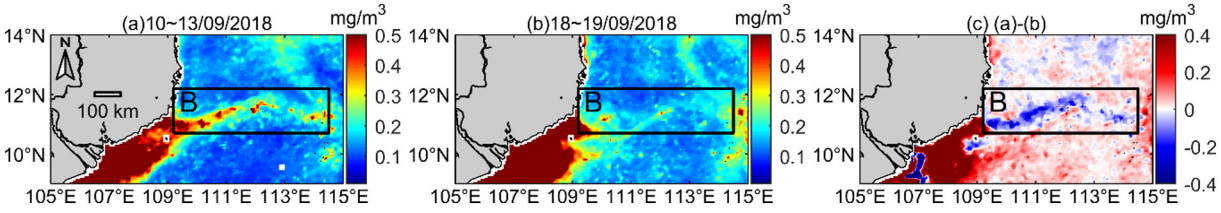

Fig. 9. Variation in the chl-a concentration in region III before and after typhoon Mangkhut: (a) the mean chl-a concentration during September 10–13, 2018; (b) the mean chl-a concentration on September 18 and 19, 2018; (c) the chl-a concentration difference between the mean value on September 18 and 19, 2018 and the mean value during September 10–13, 2018.

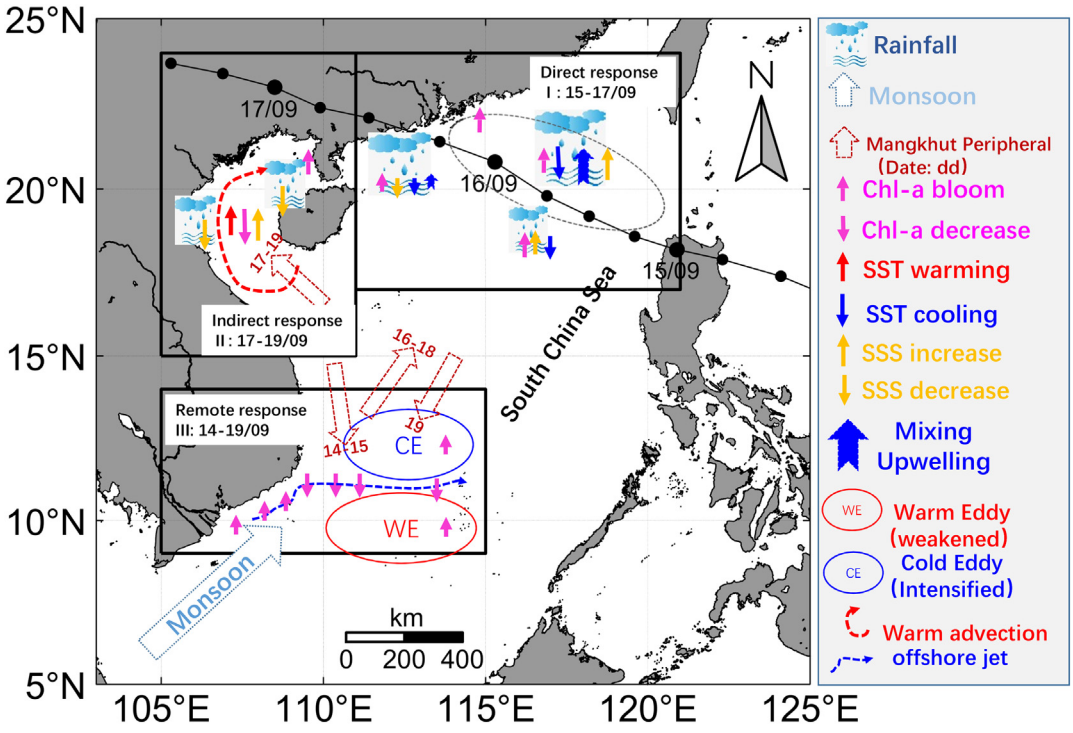

Fig. 10. Schematic diagram of the impact of super Mangkhut Typhoon on the upper ocean of the SCS.

In area II (BBG), unlike the open ocean, the response of the ocean in the semi-enclosed BBG was indirectly affected by typhoon Mangkhut. The anomalous southerly wind vector when Mangkhut landed on September 17–19, 2018, changed the original wind field in the Gulf, leading to the high-SST (>29.5 °C), low-chl-a (<0.1 mg·m^{-3}) and high-SSS (>33.5 psu) seawater outside of the BBG being transported along the anticyclonic current into the interior of the BBG (Fig. 10). This mainly caused the increase of SST is about 0.5 °C, the maximum increase of SSHA is about 20 cm, the SSS increases slightly, and chl-a decreased by 0.2 mg·m^{-3}, in the BBG. Therefore, due to the special geographical environment on three sides of the BBG, a typhoon passing in the periphery of the Gulf can also cause changes in the upper marine environment by changing the sea surface flow field.

Area III (southwest SCS) was still affected by typhoon Mangkhut even though it was far from the center of the typhoon. The abnormal wind vectors generated by Mangkhut were inversely coupled with the monsoon vectors, causing the offshore Ekman transport in the Mekong Estuary in southern Vietnam to gradually weaken and ultimately disappear. In addition, the peripheral winds of Mangkhut also intensified (weakened) and shifted the cold (warm) eddy to the north (south), blocking the eastward transportation of high-concentration chl-a (>0.3 mg·m^{-3}). These factors eventually led to the accumulation of high-value chl-a exceeding 0.4 mg·m^{-3} in the nearshore areas and the disappearance of the high-value chl-a jet.

4.2. Discussions

As well known, in the tropical oceans, especially for deep basin areas of the SCS, limited nutrient concentrations in the upper ocean are not conducive to enhancing primary productivity, which can be indicated by the variations in chl-a concentrations in phytoplankton (Bai et al., 2005; Lomas et al., 2012). Typhoon-induced upwelling and vertical mixing will bring relatively more phytoplankton and richer nutrients from the subsurface to the sea surface layer; and together with the usually sufficient sunshine and strong photosynthesis after the passing of a typhoon, there can be a marked increase in the surface chl-a concentration (Chacko, 2017; Lin et al., 2003; Liu et al., 2019; Ye et al., 2013). Our present findings on chl-a bloom and SST cooling along typhoon's track are highly consistent with previous studies (Lin et al., 2003; Sun et al., 2010; Shang et al., 2015), which is an important driving factor for enhancing primary productivity in the SCS. More importantly, we have revealed some new knowledges in typhoon wind-pump induced upper ocean response processes, which exhibits dramatically regional disparities in the basin-scale SCS. That is, there are not only a locally direct biophysical response along the typhoon track, but also an indirect response altering the environment of Beibu Gulf via Mangkhut-induced horizontal advection, and even a remote response of offshore upwelling in the southwest SCS via the opposite wind vector coupling of Mangkhut and the monsoon.

In the context of global warming, particularly, observations show that the number of typhoons generated in the SCS has decreased in the past 40 years, while typhoons on the eastern coast of the mainland have increased (Lee et al., 2012; Walsh et al., 2016). The life cycle of a typhoon is about ten days, and its impacts can reach thousands of kilometers, probably resulting in large-scale impact (Mei et al., 2015b). Although the total number of typhoons has decreased, the number of strong typhoons has tended to increase. Particularly, Mei and Xie (2016) revealed that typhoons that strike Southeast Asia have intensified by 12–15% during the past 37 years, and the proportion of typhoons of categories 4 and 5 had doubled at least (Mei and Xie, 2016). Our findings suggest that, typhoons, especially super typhoons, could in reality affect a wider area than we originally expected. Therefore, the potential increasing impacts of more frequent super typhoon-induced changes in regional marine biochemistry should be further paid attention to under global warming scenario.

In summary, for the SCS at the basin scale, super typhoons can cause anomalies in the upper marine area of the ocean over a large area (or even the entire basin). Our findings have important implications in that the impacts of typhoons on upper-ocean physics and the ecological environment are clearly multifaceted and therefore need to be further studied. Our research demonstrates the different roles of typhoon activities in different ocean region with the sea-atmosphere coupling, and may also provide insights into the interaction among different spheres of the earth. It would be worthwhile using multi-source satellite

observations and ocean model methods to explore more super typhoon cases in future work to fully understand the climatic-state impact of super typhoons on the marine environment of the SCS. In addition, the results presented in this paper have important implications for typhoon responses in other basin areas (e.g., the Gulf of Mexico).

CRediT authorship contribution statement

Shuhong Liu: Methodology, Data curation, Formal analysis, Writing - original draft, Writing - review & editing.**Jiagen Li:**Data curation, Writing - review & editing.**Liang Sun:**Methodology, Formal analysis, Writing - review & editing.**Guihua Wang:**Writing - review & editing.**Danling Tang:**Writing - review & editing.**Ping Huang:**Writing - review & editing.**Hong Yan:**Writing - review & editing.**Si Gao:**Writing - review & editing.**Chao Liu:**Writing - review & editing.**Zhiqiu Gao:**Writing - review & editing.**Yubin Li:**Writing - review & editing.**Yuanjian Yang:**Conceptualization, Methodology, Formal analysis, Writing - review & editing.

Declaration of competing interest

The authors declare that they have no known competing financial interests or personal relationships that could have appeared to influence the work reported in this paper.

Acknowledgements

This work was supported by the National Key Research and Development Program of Ministry of Science and Technology of China (2018YFC1506405), National Program on Global Change and Air–Sea Interaction (GASI-IPOVAI-04), National Foundation of Natural Science of China (No. 41876013 and 41675009), Foundation of Natural Science of Guangdong (No. 2019BT02H594), Open Funding of Guangdong Key Laboratory of Ocean Remote Sensing (2017B030301005-LORS2001), and Open Funding of State Key Laboratory of Loess and Quaternary Geology (SKLLQG1842). We thank Remote Sensing Systems for the SST and SSW data (http://www.remss.com/), Japan Aerospace Exploration Agency for the chl-a concentration product (https://www.eorc.jaxa.jp/ptree/index.html), National Aeronautics and Space Administration's Precipitation Processing System for the Integrated Multi-satellite Retrievals for GPM final precipitation product (https://pmm.nasa.gov/data-access/downloads/gpm), Copernicus Marine and Environmental Monitoring Service Center for the SSS data (http://marine.copernicus.eu/services-portfolio/access-to-products/), and Archiving, Validation and Interpretation of Satellite Oceanographic for the SSHA and Geostrophic Velocity data (https://www.aviso.altimetry.fr/en/data/products/).

Appendix A. Acronyms

Acronyms	Full name
BBG	Beibu Gulf
CE	Cold eddy
chl-a	Chlorophyll-a (unit: $mg \cdot m^{-3}$)
CMEMS	Copernicus Marine and Environmental Monitoring Service
GPM	Global Precipitation Measurement
LST	Local standard time (LST = UTC + 8)
MW_IR_OI	Microwave and infrared optimally-interpolated
NWP	Northwest Pacific
RSS	Remote sensing systems
SCS	South China Sea
SSHA	Sea surface height anomaly (unit: cm)
SSS	Sea surface salinity (unit: psu)
SST	Sea surface temperature (unit: °C)
SSW	Sea surface wind (unit: m/s)
TRMM	Tropical rainfall measuring mission
UTC	Coordinated universal time
upw	Upwelling caused by Ekman pumping (unit: m/s)
WE	Warm eddy

Appendix B. Supplementary data

Supplementary data to this article can be found online at https://doi.org/10.1016/j.scitotenv.2020.139093.

References

Abdulrazzaq, Z.T., Hasan, R.H., Aziz, N.A., 2019. Integrated TRMM data and standardized precipitation index to monitor the meteorological drought. Civil Engineering Journal 5 (7), 1590–1598.
Bai, Y., Pan, D., Guan, W., He, X., 2005. Ocean primary production estimate of China Sea by HY-1A/COCTS. Proc. SPIE 5832 (2), 406–412.
Black, P.G., D'Asaro, E.A., Drennan, W.M., French, J.R., Zhang, J.A., 2007. Air–sea exchange in hurricanes: synthesis of observations from the coupled boundary layer air–sea transfer experiment. Bull. Amer. Meteor. Soc. 88, 357–374.
Chacko, N., 2017. Chlorophyll bloom in response to tropical cyclone Hudhud in the Bay of Bengal: bio-argo subsurface observations. Deep-Sea Res. Pt. I 124, 66–72.
Chacko, N., 2018. Insights into the haline variability induced by cyclone Vardah in the Bay of Bengal using SMAP salinity observations. Remote Sens. Lett. 9 (12), 1205–1213.
Cham, D.D., Son, N.T., Minh, N.Q., Thanh, N.T., Dung, T.T., 2020. An analysis of shoreline changes using combined multitemporal remote sensing and digital evaluation model. Civil Engineering Journal 6 (1), 1–10.
Chan, K.T., Chan, J.C., Wong, W.K., 2019. Rainfall asymmetries of landfalling tropical cyclones along the South China coast. Meteorol. Appl. 26 (2), 213–220.
Chang, Y., Liao, H.T., Lee, M.A., Chan, J.W., Lan, Y.C., 2008. Multisatellite observation on upwelling after the passage of typhoon hai-tang in the southern East China Sea. Geophys. Res. Lett. 35 (3), 154–175.
Chen, Y., Tang, D., 2011. Remote sensing analysis of impact of typhoon on environment in the sea area south of Hainan Island. Procedia Environ. Sci. 10, 1621–1629.
Chen, C., Lai, Z., Beardsley, R.C., Xu, Q., Lin, H., Viet, N.T., 2012. Current separation and upwelling over the southeast shelf of Vietnam in the South China Sea. J. Geophys. Res. 117 (C3). https://doi.org/10.1029/2011JC007150.
Cheng, S.F., Cheng, C.W., Hsieh, W.C., Chi, M.C., Lin, S.J., Liao, Y.T., 2012. Effects of individual resilience intervention on indigenous people who experienced Typhoon Morkot in Taiwan. Kaohsiung J. Med. Sci. 28 (2), 105–110.
Chiang, T.L., Wu, C.R., Oey, L.Y., 2011. Typhoon Kai-Tak: an ocean's perfect storm. J. Phys. Oceanogr. 41 (1), 221–233.
Chu, P.C., Veneziano, J.M., Fan, C., Carron, M.J., Liu, W.T., 2000. Response of the South China Sea to tropical cyclone Ernie 1996. J. Geophys. Res. 105 (C6), 13991–14009.
Corbosiero, K.L., Molinari, J., 2003. The relationship between storm motion, vertical wind shear, and convective asymmetries in tropical cyclones. J. Atmos. Sci. 60 (2), 366–376.
Da, N.D., Herrmann, M., Morrow, R., Nio, F., Huan, N.M., Trinh, N.Q., 2019. Contributions of wind, ocean intrinsic variability and ENSO to the interannual variability of the South Vietnam upwelling: a modeling study. J. Geophys. Res. 124. https://doi.org/10.1029/2018JC014647.
Dippner, J.W., Nguyen, K.V., Hein, H., Ohde, T., Loick, N., 2007. Monsoon-induced upwelling off the Vietnamese coast. Ocean Dynam 57 (1), 46–62.
Donelan, M.A., Haus, B.K., Reul, N., Plant, W.J., Stiassnie, M., Graber, H.C., Brown, O.B., Saltzman, E.S., 2004. On the limiting aerodynamic roughness of the ocean in very strong winds. Geophys. Res. Lett. 31, L18306. https://doi.org/10.1029/2004GL019460.
Doong, D.J., Chuang, H.C., Shieh, C.L., Hu, J.H., 2011. Quantity, distribution, and impacts of coastal driftwood triggered by a typhoon. Mar. Pollut. Bull. 62 (7), 1446–1454.
Foltz, G.R., Balaguru, K., Leung, L.R., 2015. A reassessment of the integrated impact of tropical cyclones on surface chlorophyll in the western subtropical North Atlantic. Geophys. Res. Lett. 42, 1158–1164.
Fumin, R., Gleason, B., Easterling, D., 2002. Typhoon impacts on China's precipitation during 1957-1996. Adv. Atmos. Sci. 19 (5), 943–952.
Gao, S., Chiu, L.S., 2010. Surface latent heat flux and rainfall associated with rapidly intensifying tropical cyclones over the western North Pacific. Int. J. Remote Sens. 31 (17–18), 4699–4710.
Gao, S., Zhai, S., Li, T., Chen, Z., 2018. On the asymmetric distribution of shear-relative typhoon rainfall. Meteorol. Atmo. Phys. 130 (1), 11–22.
Gholami, D.M., Baharlouii, M., 2019. Monitoring long-term mangrove shoreline changes along the northern coasts of the Persian Gulf and the Oman Sea. Emerging Science Journal 3 (2), 88–100.
Gierach, M.M., Subrahmanyam, B., 2008. Biophysical responses of the upper ocean to major gulf of Mexico hurricanes in 2005. J. Geophys. Res. 113 (C4). https://doi.org/10.1029/2007JC004419.
Guan, X., Ma, J., Huang, J., Huang, R., Zhang, L., Ma, Z., 2019. Impact of oceans on climate change in drylands. Sci. China Earth Sci. 62, 891–908.
Han, G., Ma, Z., Chen, D., Deyoung, B., Chen, N., 2012. Observing storm surges from space: hurricane Igor off Newfoundland. Sci. Rep. 2 (12), 1010. https://doi.org/10.1038/srep01010.
Han, G., Ma, Z., Chen, N., Yang, J., Chen, D., 2017. Hurricane isaac storm surges off Florida observed by jason-1 and jason-2 satellite altimeters. Remote Sens. Environ. 198, 244–253.

Huang, S.M., Oey, L.Y., 2015. Right-side cooling and phytoplankton bloom in the wake of a tropical cyclone. J. Geophys. Res. 120 (8), 5735–5748.
Jaimes, B., Shay, L.K., 2015. Enhanced wind-driven downwelling flow in warm oceanic eddy features during the intensification of Tropical Cyclone Isaac (2012): observations and theory. J. Phys. Oceanogr. 45 (6), 1667–1689.
Kuo, N.J., Zheng, Q., Ho, C.R., 2000. Satellite observation of upwelling along the western coast of the South China Sea. Remote Sens. Environ. 74 (3), 463–470.
Kuriqi, A., 2016. Assessment and quantification of meteorological data for implementation of weather radar in mountainous regions. Mausam 67 (4), 789–802.
Lagmay, A.M.F., Agaton, R.P., Bahala, M.A.C., Briones, J.B.L.T., Cabacaba, K.M.C., Caro, C.V.C., Dasallas, L.L., Gonzalo, L.A.L., Ladiero, C.N., Lapidez, J.P., Mungcal, M.T.F., Puno, J.V.R., Ramos, M.M.A.C., Santiago, J., Suarez, J.K., Tablazon, J.P., 2015. Devastating storm surges of typhoon Haiyan. Int. J. Disast. Risk Re. 11, 1–12.
Lee, T.C., Knutson, T.R., Kamahori, H., Ying, M., 2012. Impacts of climate change on tropical cyclones in the western North Pacific basin. Part I: past observations. Tropical Cyclone Research and Review 1 (2), 213–235.
Li, Q., Sun, L., Liu, S., 2014. A new mononuclear eddy identification method with simple splitting strategies. Remote Sens. Lett. 5, 65–72.
Li, Q., Sun, L., Lin, S., 2016. GEM: a dynamic tracking model for mesoscale eddies in the ocean. Ocean Sci. 12, 1249–1267.
Lin, I.I., 2012. Typhoon-induced phytoplankton blooms and primary productivity increase in the western North Pacific subtropical ocean. J. Geophys. Res. 117 (C3). https://doi.org/10.1029/2011JC007626.
Lin, I.I., Liu, W.T., Wu, C.C., Wong, G.T.F., Hu, C., Chen, Z., Liang, W.D., Yang, Y., Liu, K.K., 2003. New evidence for enhanced ocean primary production triggered by tropical cyclone. Geophys. Res. Lett. 30 (13). https://doi.org/10.1029/2003GL017141.
Lin, I.I., Wu, C.C., Emanuel, K.A., Lee, I.H., Wu, C.R., Pun, I.F., 2005. The interaction of Supertyphoon Maemi (2003) with a warm ocean eddy. Mon. Weather Rev. 133 (9), 2635–2649.
Lin, I.I., Wu, C.C., Pun, I.F., Ko, D.S., 2008. Upper-ocean thermal structure and the western North Pacific category 5 typhoons. Part I: ocean features and the category 5 typhoons' intensification. Mon. Weather Rev. 136, 3288–3306.
Liu, X., Wang, M., 2016. Analysis of ocean diurnal variations from the Korean geostationary ocean color imager measurements using the DINEOF method. Estuar. Coast. Shelf S. 180, 230–241.
Liu, L.L., Wang, W., Huang, R.X., 2008. The mechanical energy input to the ocean induced by tropical cyclones. J. Phys. Oceanogr. 38, 1253–1266.
Liu, X., Wang, M., Shi, W., 2009. A study of a Hurricane Katrina-induced phytoplankton bloom using satellite observations and model simulations. J. Geophys. Res. 114 (C3). https://doi.org/10.1029/2008JC004934.
Liu, S.S., Sun, L., Wu, Q., Yang, Y.J., 2017. The responses of cyclonic and anticyclonic eddies to typhoon forcing: the vertical temperature-salinity structure changes associated with the horizontal convergence/divergence. J. Geophys. Res. 122 (6), 4974–4989.
Liu, Y., Tang, D., Evgeny, M., 2019. Chlorophyll concentration response to the typhoon wind-pump induced upper ocean processes considering air-sea heat exchange. Remote Sens. 11 (15), 1825. https://doi.org/10.3390/rs11151825.
Lomas, M.W., Moran, S.B., Casey, J.R., Bell, D.W., Tiahlo, M., Whitefield, J., Kelly, R.P., Mathis, J.T., Cokelet, E.D., 2012. Spatial and seasonal variability of primary production on the Eastern Bering Sea shelf. Deep-Sea Res. Pt. II 65, 126–140.
McCreary Jr., J.P., Kohler, K.E., Hood, R.R., Smith, S., Kindle, J., Fischer, A.S., Weller, R.A., 2001. Influences of diurnal and intraseasonal forcing on mixed-layer and biological variability in the central Arabian Sea. J. Geophys. Res. 106 (C4), 7139–7155.
Mei, W., Pasquero, C., 2013. Spatial and temporal characterization of sea surface temperature response to tropical cyclones. J. Clim. 26 (11), 3745–3765.
Mei, W., Xie, S.P., 2016. Intensification of landfalling typhoons over the northwest pacific since the late 1970s. Nat. Geosci. 9 (10). https://doi.org/10.1038/ngeo2792.
Mei, W., Lien, C.C., Lin, I.I., Xie, S.P., 2015a. Tropical cyclone-induced ocean response: a comparative study of the South China Sea and tropical Northwest Pacific. J. Clim. 28 (15), 5952–5968.
Mei, W., Xie, S.P., Primeau, F., McWilliams, J.C., Pasquero, C., 2015b. Northwestern pacific typhoon intensity controlled by changes in ocean temperatures. Sci. Adv. https://doi.org/10.1126/sciadv.1500014.
Murakami, H., 2016. Ocean color estimation by Himawari-8/AHI. Proc. SPIE 9878, 987810. https://doi.org/10.1117/12.2225422.
Picado, A., Lorenzo, M.N., Alvarez, I., Decastro, M., Vaz, N., Dias, J.M., 2016. Upwelling and Chl-a spatiotemporal variability along the Galician coast: dependence on circulation weather types. Int. J. Climatol. 36 (9), 3280–3296.
Powell, M.D., Vickery, P.J., Reinhold, T.A., 2003. Reduced drag coefficient for high wind speeds in tropical cyclones. Nature 422 (6929), 279–283. https://doi.org/10.1038/nature01481.
Price, J.F., 1981. Upper ocean response to a hurricane. J. Phys. Oceanogr. 11 (2), 153–175.
Price, J.F., Sanford, T.B., Forristall, G.Z., 1994. Forced stage response to a moving hurricane. J. Phys. Oceanogr. 24 (2), 233–260.
Ramos, A.M., Pires, A.C., Sousa, P.M., Trigo, R.M., 2013. The use of circulation weather types to predict upwelling activity along the western Iberian Peninsula coast. Cont. Shelf Res. 69, 38–51.
Sanford, T.B., Price, J.F., Girton, J.B., Webb, D.C., 2007. Highly resolved observations and simulations of the ocean response to a hurricane. Geophys. Res. Lett. 34, L13604. https://doi.org/10.1029/2007GL029679.
Shang, S., Li, L., Sun, F., Wu, J., Hu, C., Chen, D., Ning, X., Qiu, Y., Zhang, C., Shang, S., 2008. Changes of temperature and bio-optical properties in the South China Sea in response to Typhoon Lingling, 2001. Geophys. Res. Lett. 35 (10). https://doi.org/10.1029/2008GL033502.
Shang, X.D., Zhu, H.B., Chen, G.Y., Xu, C., Yang, Q., 2015. Research on cold core eddy change and phytoplankton bloom induced by typhoons: case studies in the South China Sea. Adv. Meteorol. 2015. https://doi.org/10.1155/2015/340432.
Shay, L.K., Goni, G.J., Black, P.G., 2000. Effects of a warm oceanic feature on Hurricane Opal. Mon. Weather Rev. 128 (5), 1366–1383.
Shi, W., Wang, M., 2007. Observations of a Hurricane Katrina-induced phytoplankton bloom in the Gulf of Mexico. Geophys. Res. Lett. 34 (11). https://doi.org/10.1029/2007GL029724.
Shi, W., Wang, M., 2011. Satellite observations of asymmetrical physical and biological responses to Hurricane Earl. Geophys. Res. Lett. 38 (4). https://doi.org/10.1029/2010GL046574.
Shibano, R., Yamanaka, Y., Okada, N., Chuda, T., Suzuki, S., Niino, H., Toratani, M., 2011. Responses of marine ecosystem to typhoon passages in the western subtropical North Pacific. Geophys. Res. Lett. 38 (18). https://doi.org/10.1029/2011GL048717.
Siswanto, E., Ishizaka, J., Morimoto, A., Tanaka, K., Okamura, K., Kristijono, A., Saino, T., 2008. Ocean physical and biogeochemical responses to the passage of Typhoon Meari in the East China Sea observed from Argo float and multiplatform satellites. Geophys. Res. Lett. 35 (15). https://doi.org/10.1029/2008gl035040.
Solanki, H.U., Mankodi, P.C., Dwivedi, R.M., Nayak, S.R., 2008. Satellite observations of main oceanographic processes to identify ecological associations in the Northern Arabian Sea for fishery resources exploration. Hydrobiologia 612 (1), 269. https://doi.org/10.1007/s10750-008-9496-8.
Subrahmanyam, M.V., 2015. Impact of typhoon on the north-west pacific sea surface temperature: a case study of typhoon kaemi (2006). Nat. Hazards 78 (1), 569–582.
Subrahmanyam, B., Rao, K.H., Rao, N.S., Murty, V.S.N., 2002. Influence of a tropical cyclone on chlorophyll-a concentration in the Arabian Sea. Geophys. Res. Lett. 29 (22), 2065. https://doi.org/10.1029/2002GL015892.
Sun, L., Yang, Y.J., Xian, T., Lu, Z., Fu, Y.F., 2010. Strong enhancement of chlorophyll a concentration by a weak typhoon. Mar. Ecol. Prog. Ser. 404, 39–50.
Sun, L., Yang, Y.J., Xian, T., Wang, Y., Fu, Y.F., 2012. Ocean responses to Typhoon Namtheun explored with Argo floats and multiplatform satellites. Atmosphere-Ocean 50 (supl 1), 15–26.
Sun, L., Li, Y.X., Yang, Y.J., Wu, Q.Y., Chen, X.T., Li, Q.Y., Li, Y.B., Tao, X., 2014. Effects of super typhoons on cyclonic ocean eddies in the western North Pacific: a satellite data-based evaluation between 2000 and 2008. J. Geophys. Res. 119 (9), 5585–5598.
Sun, W., Dong, C., Tan, W., He, Y., 2019. Statistical characteristics of cyclonic warm-core eddies and anticyclonic cold-core eddies in the North Pacific based on remote sensing data. Remote Sens. 11 (2), 208. https://doi.org/10.3390/rs11020208.
Tang, D., Kawamura, H., Lee, M.A., Dien, T.V., 2003. Seasonal and spatial distribution of chlorophyll-a concentrations and water conditions in the Gulf of Tonkin, South China Sea. Remote Sens. Environ. 85 (4), 475–483.
Tang, D., Kawamura, H., Dien, T.V., Lee, M.A., 2004a. Offshore phytoplankton biomass increase and its oceanographic causes in the South China Sea. Mar. Ecol. Prog. Ser. 268, 31–41. https://doi.org/10.3354/meps268031.
Tang, D., Kawamura, H., Doan-Nhu, H., Takahashi, W., 2004b. Remote sensing oceanography of a harmful algal bloom off the coast of southeastern Vietnam. J. Geophys. Res. 109 (C3). https://doi.org/10.1029/2003JC002045.
Tang, D., Kawamura, H., Shi, P., Takahashi, W., Guan, L., Shimada, T., Sakaida, F., Isoguchi, O., 2006. Seasonal phytoplankton blooms associated with monsoonal influences and coastal environments in the sea areas either side of the Indochina Peninsula. J. Geophys. Res. 111 (G1). https://doi.org/10.1029/2005JG000050.
Tang, D., Yu, J., Wang, S., Pan, G., 2014. Typhoon impacts on fishery in the South China Sea. Typhoon Impact and Crisis Management 40, 283–309.
Tu, J.Y., Chou, C., Huang, P., Huang, R., 2011. An abrupt increase of intense typhoons over the western North Pacific in early summer. Environ. Res. Lett. 6 (3), 034013. https://doi.org/10.1088/1748-9326/6/3/034013.
Vickery, P.J., Wadhera, D., Powell, M.D., Chen, Y., 2009. A hurricane boundary layer and wind field model for use in engineering applications. J. Appl. Meteor. Climatol. 48, 381–405.
Wada, A., Tsuguti, H., Okamoto, K., Seino, N., 2019. Air-sea coupled data assimilation experiment for Typhoons Kilo, Etau and the September 2015 Kanto-Tohoku heavy rainfall with the advanced microwave scanning radiometer 2 sea surface temperature. J. Meteorol. Soc. Jpn. 97 (3), 553–575.
Walsh, K.J.E., McBride, J.L., Klotzbach, P.J., Balachandran, S., Camargo, S.J., Holland, G., Knutson, T.R., Kossin, J.P., Lee, T.C., Sobel, A., Sugi, M., 2016. Tropical cyclones and climate change. WIRES: Clim. Change 7 (1), 65–89.
Wang, G., Chen, D., Su, J., 2006. Generation and life cycle of the dipole in the South China. Sea summer circulation. J. Geophys. Res. 111 (C6). https://doi.org/10.1029/2005JC003314.
Wang, G., Su, J., Ding, Y., Chen, D., 2007. Tropical cyclone genesis over the South China Sea. J. Marine. Syst. 68 (3–4), 318–326.
Wang, G., Ling, Z., Wang, C., 2009. Influence of tropical cyclones on seasonal ocean circulation in the South China Sea. J. Geophys. Res. 114 (C10). https://doi.org/10.1029/2009JC005302.
Wang, M., Ahn, J.H., Jiang, L., Shi, W., Son, S.H., Park, Y.J., Ryu, J.H., 2013. Ocean color products from the korean geostationary ocean color imager (GOCI). Opt. Express 21 (3), 3835–3849.
Wang, M., Son, S., Jiang, L., Shi, W., 2014. Observations of ocean diurnal variations from the Korean geostationary ocean color imager (GOCI). Proc. SPIE 9111, 911102. https://doi.org/10.1117/12.2053476.
Wang, D., Wang, Q., Cai, S., Cai, S., Shang, X., Peng, S., Shu, Y., Xiao, J., Xie, X.H., Zhang, Z., Liu, Z., Lan, J., Chen, D., Xue, H., Wang, G., Gan, J., Xie, X.N., Zhang, R., Chen, H., Yang, Q., 2019. Advances in research of the mid-deep South China Sea circulation. Sci. China Earth Sci. 62. https://doi.org/10.1007/s11430-019-9546-3.
Wentz, F.J., Gentemann, C., Smith, D., Chelton, D., 2000. Satellite measurements of sea surface temperature through clouds. Science 288 (5467), 847–850.
Xie, S.P., Xie, Q., Wang, D., Liu, W.T., 2003. Summer upwelling in the South China Sea and its role in regional climate variations. J. Geophys. Res. 108 (C8). https://doi.org/10.1029/2003JC001867.

Xie, S.P., Chang, C.H., Xie, Q., Wang, D.X., 2007. Intraseasonal variability in the summer South China Sea: wind jet, cold filament, and recirculations. J. Geophys. Res. 112 (C10). https://doi.org/10.1029/2007JC004238.

Xu, Y., Wang, Z., 2017. Response of surface ocean conditions to Typhoon Rammasun (2014). J. Coastal Res 80 (sp1), 92–97.

Yang, Y.J., Sun, L., Liu, Q., Xian, T., Fu, Y.F., 2010. The biophysical responses of the upper ocean to the Typhoons Namtheun and Malou in 2004. Int. J. Remote Sens. 31 (17–18), 4559–4568.

Yang, Y.J., Sun, L., Duan, A.M., Li, Y.B., Fu, Y.F., Yan, Y.F., 2012a. Impacts of the binary typhoons on upper ocean environments in November 2007. J. Appl. Remote. Sens. 6 (1), 063583. https://doi.org/10.1117/1.JRS.6.063583.

Yang, Y.J., Xian, T., Sun, L., Fu, Y.F., 2012b. Summer monsoon impacts on chlorophyll-a concentration in the middle of the South China Sea: climatological mean and annual variability. Atmos. Oceanic Sci. Lett. 5 (1), 15–19.

Yang, Y.J., Wang, H., Chen, F.J., Zheng, X.Y., Fu, Y.F., Zhou, S.X., 2019. TRMM-based optical and microphysical features of precipitating clouds in summer over the Yangtze-Huaihe River Valley, China. Pure Appl. Geophys. 176 (1), 357–370.

Ye, H., Sui, Y., Tang, D., Afanasyev, Y.D., 2013. A subsurface chlorophyll a bloom induced by typhoon in the South China Sea. J. Marine. Syst. 128, 138–145.

Yu, Y., Xing, X., Liu, H., Yuan, Y., Wang, Y., Chai, F., 2019. The variability of chlorophyll-a and its relationship with dynamic factors in the basin of the South China Sea. J. Marine. Syst. 200, 103230. https://doi.org/10.1016/j.jmarsys.2019.103230.

Yue, C., Cao, Y., Gu, W., Tan, J., Li, X., 2016. Study on the genesis of asymmetrical distribution characteristics of precipitation associated with the typhoon Haitang (2005) from the view of atmospheric factor. J. Trop. Meteorol. 22 (3), 265–276.

Yue, X., Zhang, B., Liu, G., Li, X., Zhang, H., He, Y., 2018. Upper Ocean response to typhoon Kalmaegi and Sarika in the South China Sea from multiple-satellite observations and numerical simulations. Remote Sens. 10 (2), 348. https://doi.org/10.3390/rs10020348.

Zhang, S., Xie, L., Hou, Y., Zhao, H., Qi, Y., Yi, X., 2014. Tropical storm-induced turbulent mixing and chlorophyll-a enhancement in the continental shelf southeast of Hainan Island. J. Marine. Syst. 129, 405–414.

Zhao, H., Duan, X., Raga, G., Sun, F., 2018. Potential large-scale forcing mechanisms driving enhanced North Atlantic tropical cyclone activity since the mid-1990s. J. Clim. 31, 1377–1397.

Zhao, H., Tang, D., Wang, Y., 2008. Comparison of phytoplankton blooms triggered by two typhoons with different intensities and translation speeds in the South China Sea. Mar. Ecol. Prog. Ser. 365, 57–65. https://doi.org/10.3354/meps07488.

Zhao, H., Tang, D., Wang, D., 2009. Phytoplankton blooms near the Pearl River estuary induced by Typhoon Nuri. J. Geophys. Res. 114 (C12). https://doi.org/10.1029/2009JC005384.

Zheng, G.M., Tang, D., 2007. Offshore and nearshore chlorophyll increases induced by typhoon winds and subsequent terrestrial rainwater runoff. Mar. Ecol. Prog. Ser. 333, 61–74.

Zheng, Z.W., Ho, C.R., Zheng, Q., Kuo, N.J., Lo, Y.T., 2010. Satellite observation and model simulation of upper ocean biophysical response to Super Typhoon Nakri. Cont. Shelf Res. 30 (13), 1450–1457.